 doi:10.20944/preprints202205.0137.v1

Article

Spectral Analysis of Flow Around Single and Two Crossing Circular Cylinders Arranged at 60 and 90 Degrees

Tianyuan Wang[1], Qingqing Yang[1], Yeting Tang[1]†, Hongda Shi[1], Qin Zhang[1], Mengfei Wang[1] , Andrey Epikhin2 and Andrey Britov[2].

[1]College of Engineering, Ocean University of China, Qingdao, China
[2]Ivannikov Institute for System Programming of the RAS, Moscow, Russia

Abstract: Two modal decomposition techniques, including proper orthogonal decomposition (POD) and dynamic mode decomposition (DMD), are used to identify the wake patterns past single and two crossing cylinders in 60° and 90° arrangements with gap ratio $G = 4$. The flow is simulated using direct numerical simulations (DNS) for Reynolds numbers $Re = 100$. The spatial scale of flow decreases with increasing modal frequency from the modal analysis. Two main modes are identified in the wake of the cylinders, namely spatially antisymmetric and symmetric modes. Antisymmetric and symmetric modes are related to cylinders' vortex shedding and shedding vortices' shift motion, respectively, whose frequencies are odd and even multiples of cylinders' lift force frequency. In addition, a low-frequency mode concerning the shadowing effect of the downstream cylinder (DC) in 90° arrangement is found in the wake of the DC centre.

Keywords: low-dimensional models; vortex dynamics; wakes

1. Introduction

Vortex-induced vibration (VIV) of a circular cylinder has always been of interest to researchers due to its engineering applications (Jauvtis & Williamson 2003; Zhao *et al.* 2009). In particular, if the self-oscillation frequency of a downstream structure is close to the vortex shedding frequency from the upstream circular cylinder, the structure will be destroyed by resonance (Deng *et al.* 2007; Kato *et al.* 2012; Nguyen *et al.* 2012). Therefore, the relationship between wake morphologies and flow frequencies is worth studying.

The vortex shedding from a single circular cylinder is dependent on the flow direction (Jauvtis & Williamson 2003; Zhao *et al.* 2009) and Reynolds number *Re*. Different arrangements of multiple circular cylinders also affect the morphologies of the wake vortices. For two circular cylinders, parallel (including tandem, side-by-side and staggered) and crossing arrangements make the flow past the cylinders more complex (Kato *et al.* 2012; Nguyen *et al.* 2012; Sumner 2010; Tong *et al.* 2015; Zhao & Lu 2018; Zhou & Mahbub Alam 2016). For instance, if two circular cylinders are perpendicular to each other, i.e. so-called cruciform arrangement, the morphologies of the gap flow between two cylinders and vortex shedding are determined by the flow direction, gap-to-diameter ratio (defined as *G*) and Reynolds number *Re* (Zhao & Lu 2018).

Flows around circular cylinders are spatiotemporally coupled results, and it isn't easy to separate the single-frequency flows from them. Modal decomposition technologies (Taira *et al.* 2017), including proper orthogonal decomposition (POD, Lumley 1970) and dynamic mode decomposition (DMD, Schmid 2010) have been proved to be powerful methods for solving this problem and have been widely used to analyse single cylinder wake obtained via particle image velocimetry (PIV) experiments (Sakai *et al.* 2015; Tu *et al.* 2014; Wang *et al.* 2014) and numerical simulations (Bagheri 2013; Bai *et al.* 2019; Chen *et al.* 2012; Naderi *et al.* 2019; Scherl *et al.* 2020; Zhao *et al.* 2019).

For multiple cylinders in different arrangements, Zhang *et al.* (2014) conducted a comprehensive comparison on identifying coherent structures in wake flow behind two side-by-side circular cylinders of different diameters obtained by PIV. Sakai *et al.* (2014) employed POD and DMD to analyse the experimental and numerical flow around two circular cylinders in tandem and side-by-side arrangements. Sirisup & Tomkratoke (2009) performed POD on the flow around two staggered circular cylinders obtained by using direct numerical simulations (DNS). Wang *et al.* (2020) analysed the flow around two square cylinders in tandem arrangement with different G spacing ratios based on POD and DMD. Noack *et al.* (2016) proposed a variant DMD algorithm, called recursive DMD (RDMD), to analyse the wake past three rotating cylinders in staggered arrangements calculated by DNS, and the modal results are compared with that obtained by original POD and DMD methods.

The above investigations mainly employed POD and DMD in parallel cylinder flows, but little literature has focused on applying these two modal analysis methods in crossing cylinder flows. In addition, little research has been done to establish a link between POD and DMD modes and cylindrical lift and drag coefficients through frequency. Therefore, the main objective of our study is to explore the relationship between flow morphologies and frequencies. To this end, we employ POD and DMD to analyse the wake past a single circular cylinder and two crossing circular cylinders with the crossing angles $\beta = 60°$ and $90°$ and $G = 4$ (see Figure 1). This study can provide a reference for VIV in standard three-dimensional cylinder configurations.

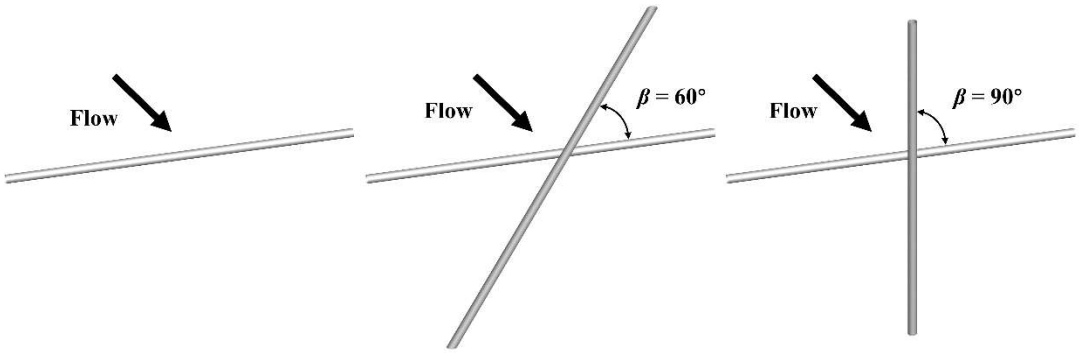

Figure 1 Sketch of single and two crossing circular cylinders configurations.

The paper is organised as follows. Section 2 presents the numerical simulation methodology, and Section 3 studies the cylindrical lift force coefficient, and spatial and spectral features of the wake at $Re = 100$. The modal decomposition results of the wake are presented in Section 4. Finally, the key results are summarised in Section 5.

2. Overview of numerical simulation

The governing equations for simulating the incompressible viscous fluid flow are the three-dimensional Navier–Stokes (NS) equations:

$$\frac{\partial u_i}{\partial x_i} = 0, \tag{1}$$

$$\frac{\partial u_i}{\partial t} + u_j \frac{\partial u_i}{\partial x_j} = -\frac{\partial p}{\partial x_i} + \frac{1}{Re} \frac{\partial^2 u_i}{\partial x_j \partial x_j}, \tag{2}$$

where x_i ($x_1 = x$, $x_2 = y$, $x_3 = z$) represents the Cartesian coordinates, u_i is the fluid velocity in the x_i direction ($u_1 = U_x$, $u_2 = U_y$, $u_3 = U_z$), t is time and p is pressure. The Reynolds number Re is defined as $Re = U_\infty D/\nu$, where ν is the kinematic viscosity of the fluid. In this study, the fluid velocity is $U_\infty = 1$ m/s in the x direction, the cylinder diameter is $D = 1$ m,

Preprints (www.preprints.org) | NOT PEER-REVIEWED | Posted: 10 May 2022 doi:10.20944/preprints202205.0137.v1

the fluid kinematic viscosity is chosen as ν = 0.01 m²/s, and the Reynolds number is Re = 100. All cases are summarized in Table 1.

Table 1. Cases in the study.

Case	Objective
Single cylinder	For spectral analysis
β = 60°, G = 4, Re = 100	For spectral analysis
β = 90°, G = 4, Re = 100	For spectral analysis
β = 90°, G = 0.5, Re = 500	For comparison only

The computational domain is a rectangular box with a length of 42D and a width and height of 40D. The length of the cylinders spans the entire computational domain. The non-dimensional gap between the two crossing cylinders is defined as $G = S/D$, where S is the spacing between two cylinders (see Figure 2). The upstream cylinder (UC) is a transversal cylinder with the centre of (0, 0 ,0) for the studied three configurations. For the crossing configurations, the centre of the downstream cylinder (DC) is (5, 0 ,0), and the crossing angle β is defined as DC's inclination angle concerning the line of (x/D, z/D) = (5, 0).

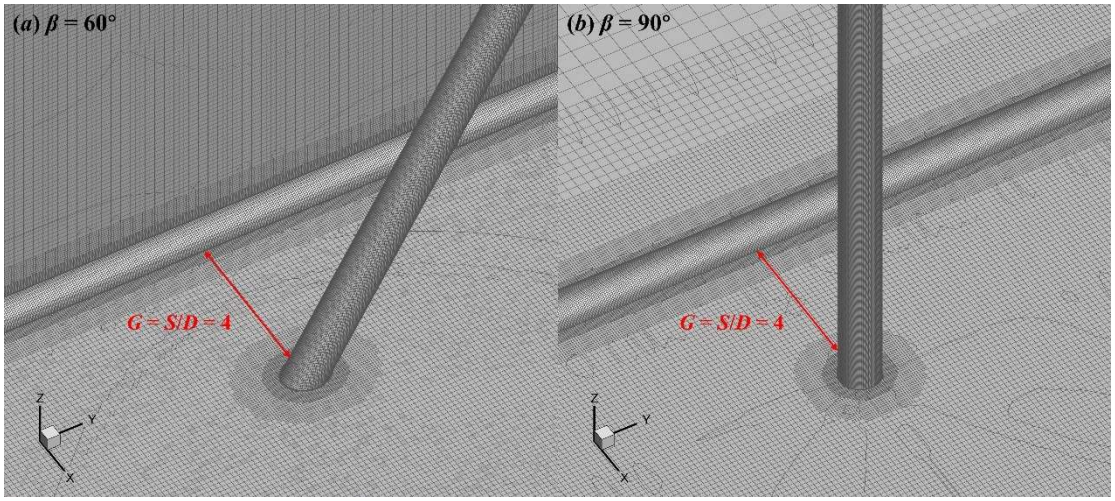

Figure 2 Computational mesh for the two crossing circular cylinders in 60° (a) and 90° (b) arrangements with G = 4.

The effect of the mesh density on the numerical results is investigated by performing the simulations on three meshes of different densities for two cylinders in cruciform arrangement (β = 90°) with G = 0.5 at Re = 500. The computational domain is discretised by the snappyHexMesh mesh generator. Figure 2 shows the computational mesh near the cylinders. The mesh information is listed in Table 2, and the comparison of mean drag coefficient $\overline{C}_D$ within $|L/D| < 3$ (L is cylinder length) and time-averaged streamwise velocity $\overline{U}_x$ along the x axis from x/D = 2 to 12 between coarse, medium and fine meshes are present in Figure 3.

Table 2. Coarse, medium and fine mesh used for mesh convergence analysis.

	Mesh number	Thickness of first layer mesh	Number of boundary layer nodes
Coarse	9 million	0.004D	48

Preprints (www.preprints.org) | NOT PEER-REVIEWED | Posted: 10 May 2022 doi:10.20944/preprints202205.0137.v1

Medium	14 million	0.002D	96
Fine	22 million	0.001D	192

The sectional drag coefficient is defined as $C_D = 2F_D/(\rho D U_\infty^2)$, where F_D is the sectional drag force calculated by integrating the pressure and shear stress along the section circumference is parallel to the inflow direction. It is clear from Figure 3 (a) that the $\overline{C}_D$ of UC calculated by the medium mesh and that of DC calculated by the fine mesh is closer to the results obtained from Mesh 1 in Zhao & Lu (2018). For the wake region, the $\overline{U}_x$ obtained from the medium mesh is similar to that of the fine mesh (Figure 3b).

Although the two largest meshes show similar convergence, we still pick up the most density one as the target mesh to ensure accuracy. Finally, the mesh numbers are 18 million, 22 million and 22 million for the cases of single cylinder, two crossing cylinders in 60° and 90° arrangements with $G = 4$, respectively. The y^+ value of each case is lower than 1. Based on the DNS, the time step of the transient simulation is set to dt = 0.005s.

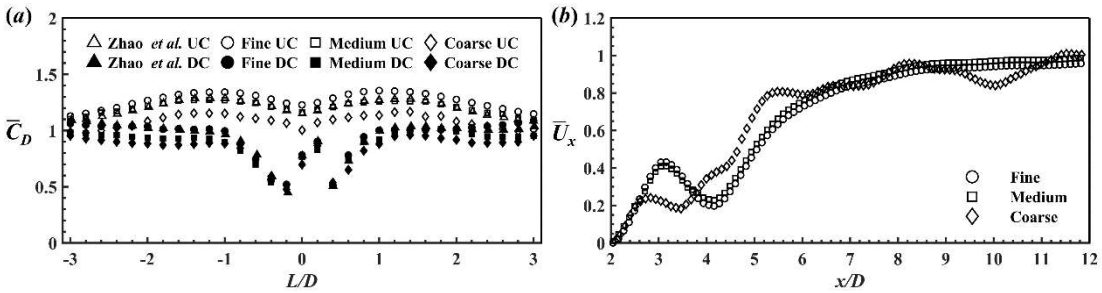

Figure 3 Comparison of mean drag coefficient (a) and time-averaged streamwise velocity along the x axis (b) between the coarse, medium and fine meshes.

3. Numerical results

The numerical results in this section focus on the lift coefficients, wake morphologies and their spectra.

3.1. Lift force coefficient

Figure 4 shows the contours of sectional lift force coefficient $C_L = 2F_L/(\rho D U_\infty^2)$ along the cylinders, where F_L is the sectional lift force and its direction is perpendicular to the inflow direction. For the single cylinder, the lift force oscillates with time, and there is no time shift of the lift force along the spanwise direction of the cylinder (Figure 4a). While for the two crossing cylinders, the lift force at the UC centre is always ahead of that at two sides of the cylinders, and the amplitude of the lift force at the UC centre is higher than that at two sides of the cylinders (see Figure 4b, c). This phenomenon also occurs in the lift force of DC in 60° arrangement and the amplitude difference is more pronounced. However, for the DC in 90° arrangement, the lift force at the DC centre is almost zero under the influence of UC.

A fast Fourier transform (FFT) is further performed on the sectional lift force coefficient to calculate lift force's power spectral density (PSD), and the contours of the Strouhal number $St_L = f_L D/U_\infty$ determined by the frequency of lift force f_L is shown in Figure 5. It is clear from Figure 5 that the lift force frequency is $St_L = 0.16$ and is not related to the inclination angle of DC. For the DC in 60° arrangement, there is a second high-frequency of $St_L = 0.32$ at the cylinder centre.

Preprints (www.preprints.org) | NOT PEER-REVIEWED | Posted: 10 May 2022 doi:10.20944/preprints202205.0137.v1

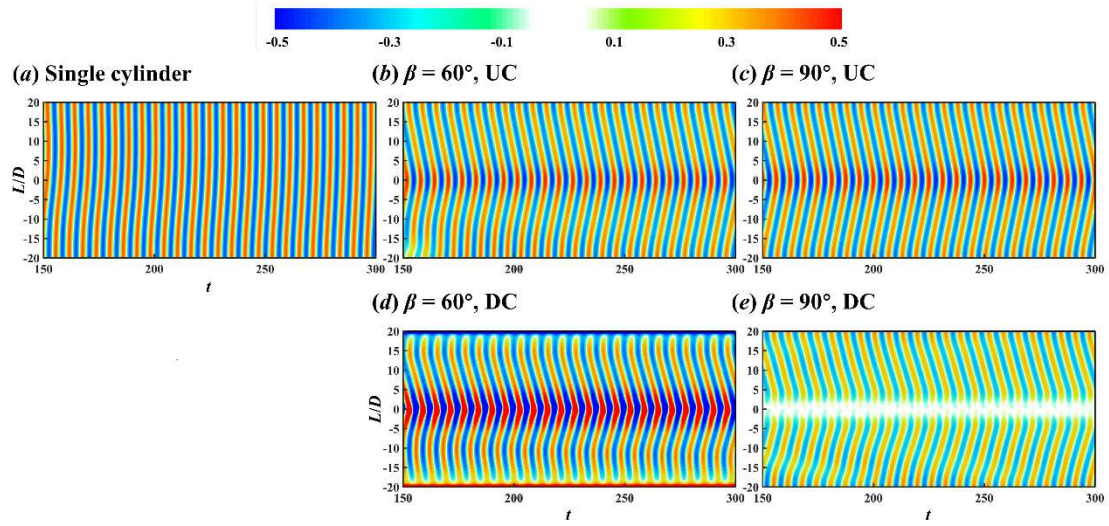

Figure 4 Contours of sectional lift coefficient along the single cylinder (*a*), and UC (*b*, *c*) and DC (*d*, *e*) for two crossing cylinders in 60° (middle) and 90° (right) arrangements.

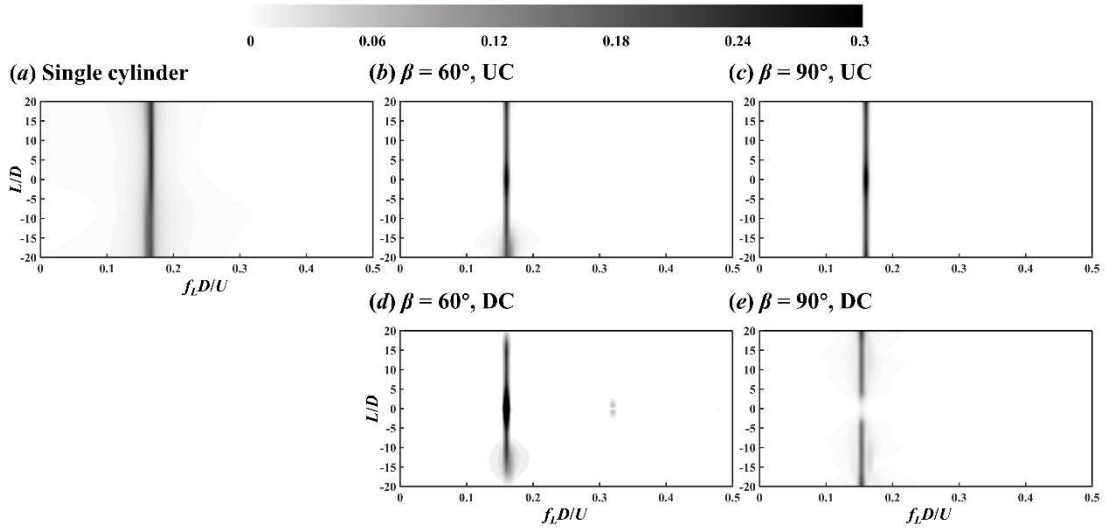

Figure 5 Contours of PSD calculated by sectional lift coefficient along the single cylinder (*a*), and UC (*b*, *c*) and DC (*d*, *e*) in 60° (middle) and 90° (right) arrangements.

3.2. Flow field

Since the lift force is related to the vortex shedding from the cylinders (Tong *et al.* 2015; Zhao & Lu 2018), the wake morphologies of the single and two crossing cylinders are presented by the λ_2 iso-surfaces (Jeong & Hussain 1995) in Figure 6. λ_2 is the second eigenvalue of the tensor $\boldsymbol{\Psi}^2+\boldsymbol{\Omega}^2$, where $\boldsymbol{\Psi}$ and $\boldsymbol{\Omega}$ are the symmetric and the anti-symmetric parts of the velocity-gradient tensor, respectively.

From a global perspective, the wake vortices shedding from the single cylinder are parallel to the cylinder, and this wake morphology is called parallel (P) mode (see Figure 6*a*). For the crossing cylinders, the vortex shedding near the centre of each cylinder lags the vortex shedding from two sides of the centre of the cylinder, forming inclined vortex morphology, i.e. K mode (see Figure 6*b*, *c*).

The vorticity magnitude $|\boldsymbol{\omega}| = |\nabla\times\boldsymbol{U}| = (\omega_x^2+\omega_y^2+\omega_z^2)^{1/2}$ contours on the *xz* and *xy* planes are presented in Figure 7 and Figure 8, respectively. The vorticity magnitude is

Preprints (www.preprints.org) | NOT PEER-REVIEWED | Posted: 10 May 2022 doi:10.20944/preprints202205.0137.v1

calculated to consider the curl of velocity in the x, y, z directions. For the gap flow, the gap ratio G is sufficiently large in this study and the vortex shedding is also generated in the gap between two crossing cylinders (Figure 7*b*, *c* and Figure 8). The alternating vortex shedding can be found in the wake of DC in 60° arrangement, but the wake vortices of DC centre in 90° arrangement remain symmetric under the influence of UC wake and DC's blockage effect (Zhao & Lu 2018).

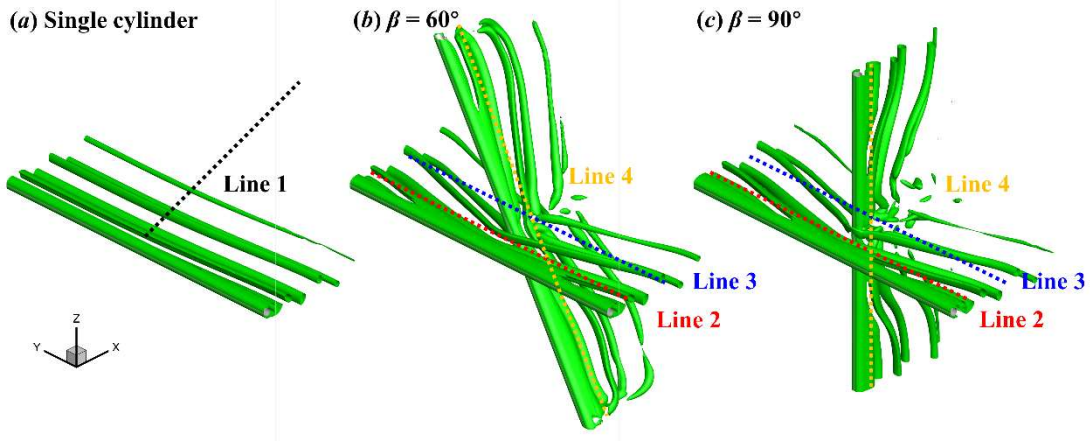

Figure 6 Flow around the single cylinder (*a*) and two crossing cylinders in 60° (*b*) and 90° (*c*) arrangements. Iso-surfaces $\lambda_2 = -0.2$.

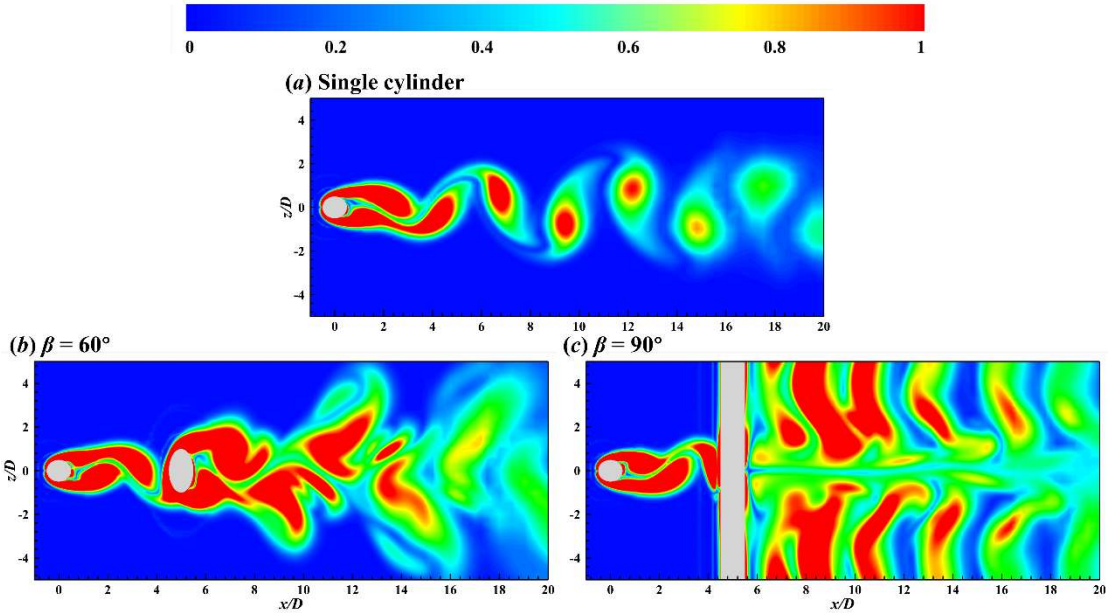

Figure 7 Contours of vorticity magnitude on the xz plane for the flow around the single cylinder (*a*) and two crossing cylinders in 60° (*b*) and 90° (*c*) arrangements. The vorticity is normalised by U_∞/D.

Preprints (www.preprints.org) | NOT PEER-REVIEWED | Posted: 10 May 2022 doi:10.20944/preprints202205.0137.v1

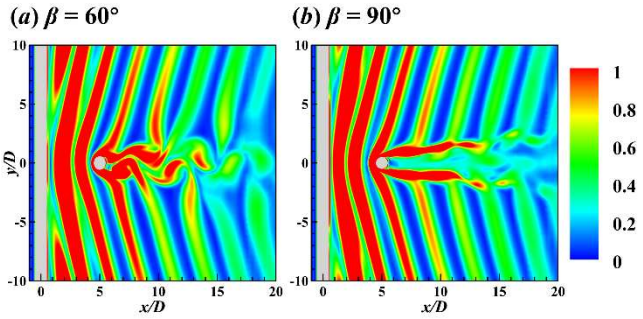

Figure 8 Contours of vorticity magnitude on the xy plane for the flow around the two crossing cylinders in 60° (b) and 90° (c) arrangements. The vorticity is normalised by U_∞/D.

A series of probes spaced at 1D interval are inserted in the wake field to record the wake velocity, as shown by lines 1 (y/D = 0, z/D = 0), 2 (x/D = 3, z/D = 0), 3 (x/D = 8, z/D = 0), 4 (x/D = 8, z/y = tan60° for β = 60° case and x/D = 8, y/D = 0 for β = 90° case) in Figure 6. Based on the wake velocity, the kinetic energy KE = $0.5(U_x^2+U_y^2+U_z^2)$ in the wake is obtained and the PSD of KE is calculated through FFT. Figure 9 presents the energy evolution in the wake of the single cylinder along the x axis from x/D = 1 to 30, and Figure 10 shows the flow frequencies along the spanwise direction of each cylinder at different streamwise positions.

It is clear from Figure 9 that there are two distinct spectral peaks of $St_{KE} = f_{KE}D/U_\infty$ = 0.32 and 0.64, which are two and four times of lift force frequency St_L = 0.16 in Figure 5 (a), respectively. The free shear layers generate the shedding vortices on left and right boundaries of a cylinder. Since the vortex shedding on one side corresponds to the peak lift force and the next vortex shedding on the other side corresponds to the valley lift force, there are two vortex shedding phenomena in one lift force period, i.e. St_{KE} = 0.32 = 2St_L. A complete vortex shedding period T is approximately 6.25s.

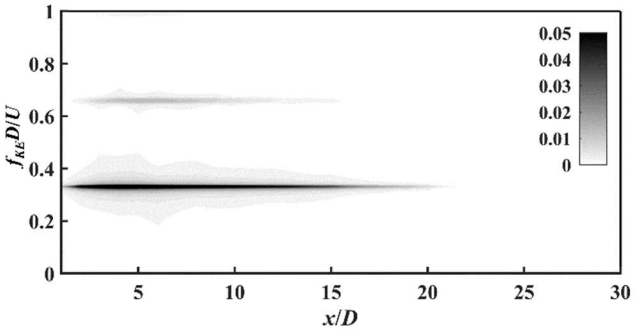

Figure 9 Contour of PSD calculated by the KE along line 1 in the wake of the single cylinder.

Similarly, multiple spectral peaks can also be found in the wake of two crossing cylinders, i.e. St_{KE} = 0.16, 0.32, 0.48 and 0.64, where St_{KE} = 0.16 and 0.48 are significant only near the crossing point. However, the spectra and flow field cannot resolve the flow morphologies corresponding to the above characteristic frequencies. Therefore, modal decomposition methods are employ to solve this problem.

Preprints (www.preprints.org) | NOT PEER-REVIEWED | Posted: 10 May 2022 doi:10.20944/preprints202205.0137.v1

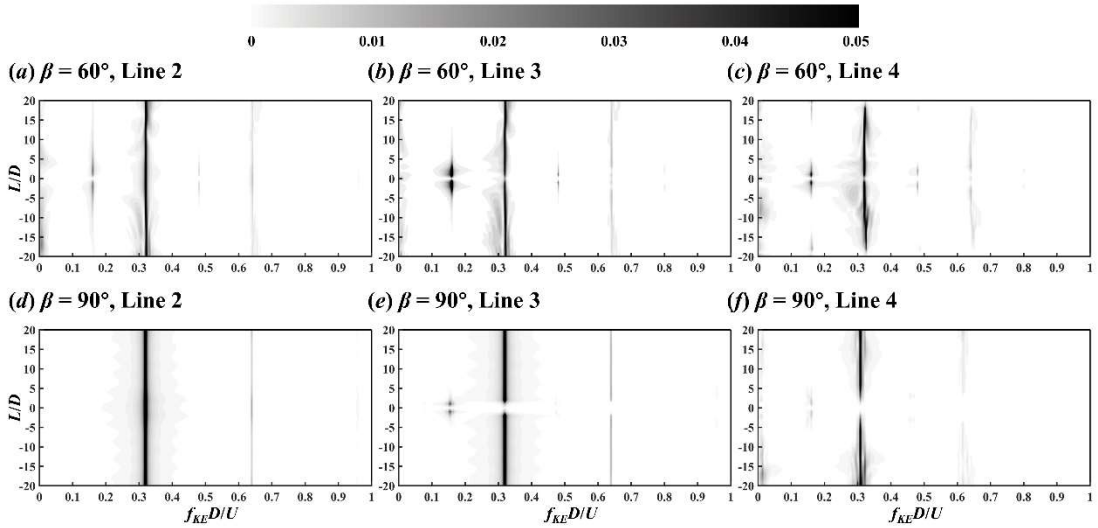

Figure 10 Contour of PSD calculated by the KE along lines 2, 3 and 4 in the wake of the two crossing cylinders in 60° (*a*, *b*, *c*) and 90° (*d*, *e*, *f*) arrangements.

4. Modal analysis

4.1. Theory

POD (Lumley 1970) and DMD (Schmid 2010) are the most useful modal analysis methods to identify the flow characteristics through dimensionality reduction decomposition. The fundamental theories of POD and DMD are briefly reviewed, while the details can be found in the cited references.

4.1.1. POD

POD is essentially an EVD method of seeking the optimal basis functions that best represent the given flow field data by solving the spatial covariance matrix $\boldsymbol{R} = \boldsymbol{X}\boldsymbol{X}^{\mathrm{T}}$ of the snapshot matrix $\boldsymbol{X}$, and is equivalent to dealing with the SVD of the snapshot matrix $\boldsymbol{X}$ in the sense of least squares (Wall *et al.* 2002; Kutz *et al.* 2016):

$$\boldsymbol{X} = \boldsymbol{U}\boldsymbol{\Sigma}\boldsymbol{V}^{\mathrm{T}}, \tag{4.1}$$

where $\boldsymbol{U} = [\boldsymbol{u}_1, \boldsymbol{u}_2, \dots, \boldsymbol{u}_m] \in \mathbb{C}^{n\times m}$ $(m \ll n)$ is the left singular (POD mode) matrix, $\boldsymbol{\Sigma} = \mathrm{diag}(\sigma_1, \sigma_2, \dots, \sigma_m) \in \mathbb{R}^{m\times m}$ is the singular value (energy) matrix, and $\boldsymbol{V} = [\boldsymbol{v}_1, \boldsymbol{v}_2, \dots, \boldsymbol{v}_m] \in \mathbb{C}^{m\times m}$ is the right singular matrix. The time coefficient $\boldsymbol{a}_i(t)$ $(i = 1, 2, \dots, m)$ of the each POD mode $\boldsymbol{u}_i$ can be obtained by multiplying its singular values σ_i with the right singular vectors $\boldsymbol{v}_i$:

$$\boldsymbol{a}_i(t) = \sigma_i \boldsymbol{v}_i^{\mathrm{T}}, \tag{4.2}$$

Each POD mode $\boldsymbol{u}_i$ is ranked according to its energy σ_i, namely each POD mode $\boldsymbol{u}_i$ is ordered by the degree to which it captures the spatial features of the flow field. The relative energy of each mode and the cumulative energy of the first ith modes are defined as

$$E_i = \frac{\sigma_i}{\sum_{j=1}^{m}\sigma_j}, \; E_i^{cum} = \sum_{k=1}^{i} E_k . \tag{4.3a, b}$$

4.1.2. DMD

The theory of DMD proposed by Schmid (2010) assumed that there is a time-invariant linear operator $\boldsymbol{A}$ between adjacent snapshots, which can be expressed in a discrete-time dynamic system as

$$\boldsymbol{X}' = \boldsymbol{A}\boldsymbol{X}, \tag{4.4}$$

Preprints (www.preprints.org) | NOT PEER-REVIEWED | Posted: 10 May 2022 doi:10.20944/preprints202205.0137.v1

where $\boldsymbol{X} = [\boldsymbol{x}_0, \boldsymbol{x}_1, \dots, \boldsymbol{x}_{m-1}] \in \mathbb{R}^{n\times m}$ and $\boldsymbol{X}' = [\boldsymbol{x}_1, \boldsymbol{x}_2, \dots, \boldsymbol{x}_m] \in \mathbb{R}^{n\times m}$ are snapshot matrices with snapshot vectors $\boldsymbol{x}_i$ ($i = 0, 1, \dots, m$) sampled at a constant time interval $\Delta t_s = t_{i+1} - t_i$ ($i = 0, 1, \dots, m - 1$). The best-fit matrix $\boldsymbol{A}$ is given by

$$\boldsymbol{A} = \boldsymbol{X}'\boldsymbol{X}^{\dagger}, \tag{4.5}$$

where $\boldsymbol{A} \in \mathbb{C}^{n\times n}$, $\dagger$ denotes the Moore-Penrose pseudoinverse, which is equivalent to seeking the best-fit solution of the matrix $\boldsymbol{A}$ in a least-squares sense.

Unlike the POD, the DMD assumes that the modes and dynamic information of the flow field are contained in the eigenvalues and eigenvectors of operator $\boldsymbol{A}$, respectively. Since the matrix $\boldsymbol{A}$ ($n\times n$) is generally too large, unaffordable computational resources would be required if the EVD is performed directly on matrix $\boldsymbol{A}$. Therefore, the effective DMD algorithm proposed by Tu *et al.* (2013) is usually employed to reduce the computational cost. Then the spatial information (eigenvector) on each DMD mode $\boldsymbol{\phi}_i$ and its eigenvalue λ_i can be obtained. The growth/decay rate g_i and frequency f_i of each DMD mode can then be denoted based on the eigenvalue λ_i as

$$g_i = \mathrm{In}(\mathrm{Re}(\lambda_i))/\Delta t_s, \tag{4.6}$$

$$f_i = \mathrm{In}(\mathrm{Re}(\lambda_i))/(2\pi\Delta t_s). \tag{4.7}$$

The amplitude (energy) α_i can be calculated based on the initial snapshot $\boldsymbol{x}_0$ as shown in Kutz *et al.* (2016):

$$\boldsymbol{\alpha} = [\alpha_1, \alpha_2, \dots, \alpha_m]^{\mathrm{T}} = \boldsymbol{\Phi}^{\dagger}\boldsymbol{x}_0, \tag{4.8}$$

where $\boldsymbol{\alpha} \in \mathbb{C}^m$ is amplitude vector and $\boldsymbol{\Phi} = [\boldsymbol{\phi}_1, \boldsymbol{\phi}_2, \dots, \boldsymbol{\phi}_m] \in \mathbb{C}^{n\times m}$ is DMD mode matrix. Each original snapshot $\boldsymbol{x}_j$ ($j = 0, 1, \dots, m$) can be approximately reconstructed by linearly superimposing r modes as

$$\boldsymbol{x}_j \approx \tilde{\boldsymbol{y}}_j = \sum_{i=1}^{r} \boldsymbol{\phi}_i a_i(t_j), \tag{4.9}$$

where $a_i(t_j)$ is the time coefficient of DMD mode $\boldsymbol{\phi}_i$ at j moment.

4.2. Raw data

In this paper, the vorticity magnitude is selected for modal decomposition, consistent with Chen *et al.* (2012), Sakai *et al.* 2014, Tu *et al.* 2014, Kutz *et al.* 2016, Noack *et al.* 2016 and Scherl *et al.* 2020. As Rowley & Dawson (2017) reported, subtracting the mean flow from the snapshot datasets makes the flow field more natural but reduces the DMD to the temporal discrete Fourier transform (DFT). The removal of the mean flow will result in each DMD mode being distributed at a same frequency interval, undoubtedly disturbing the frequencies of non-periodic modes. Therefore, the mean flow is retained in the raw datasets used for modal decomposition.

As seen from Figure 4, the lift force remains stable from 200s onwards, thus vorticity data in the last 100s (from 200 to 300s, around sixteen vortex shedding periods) are chosen for modal decomposition. The snapshot data is output at the time interval of $\Delta t = 2\mathrm{d}t = 0.01$s, corresponding to the maximum sampling frequency of $f_{max} = 1/\Delta t = 100$ Hz.

4.3. Convergence analysis

The modal convergence is dependent on the sampling time interval Δt_s and the coverage period T_s of fully developed flow field data. The sampling time interval must be sufficiently small to capture high-frequency flow features, and the coverage period must be enough to capture long-period flow features.

According to the Nyquist-Shannon criterion (Desoer & Wang 1980), the sampling frequency f_s should be at least two times flow frequency f to capture flow features in the range of 0 to f, i.e.

Preprints (www.preprints.org) | NOT PEER-REVIEWED | Posted: 10 May 2022 doi:10.20944/preprints202205.0137.v1

$$f_s = 1/\Delta t_s \geq 2f. \tag{4.10}$$

In addition, DMD is not sensitive to whether the dataset covers integral multiples of periods or not (Chen *et al.* 2012), but POD may generate spurious modes when the dataset does not cover integer number periods.

The modal convergence is determined by the root mean square error (RMSE) between the snapshot data and DMD reconstruction result at time $m + 1$, i.e. the L_2 norm of $\boldsymbol{x}_{m+1} - \tilde{\boldsymbol{y}}_{m+1}$:

$$||\boldsymbol{x}_{m+1} - \tilde{\boldsymbol{y}}_{m+1}||_2 = \sqrt{\sum_{i=1}^{n} (\boldsymbol{x}_{i,\,m+1} - \tilde{\boldsymbol{y}}_{i,\,m+1})^2}, \tag{4.11}$$

DMD can predict the next time flow field with high accuracy if all significant modes are contained.

In this study, different sampling time intervals $\Delta t_s = 3, 4, 5\Delta t = 0.03, 0.04, 0.05$s (capturing the modes in the frequency range of $0 \leq St = fD/U_\infty \leq 33.3, 12.5, 10$, respectively) and coverage periods $T_s = 1, 2, 3, 4, 5T = 6.25, 12.5, 18.75, 25, 31.25$s (covering 1 to 5 vortex shedding periods, respectively) are set to investigate the effect of sampling time interval and coverage period on modal convergence. Figure 11 illustrates the RMSE between the snapshot data and the DMD reconstruction result for the single cylinder case. The reconstruction error decreases with increasing coverage periods and the decreasing sampling interval. For $\Delta t_s = 3\Delta t$, the error reaches a plateau for $T_s = 4T$, after which it does not change significantly. Hence we consider the snapshot number $m = 1042$ ($\Delta t_s = 0.03$s, $T_s = 5.0016$s) for this study.

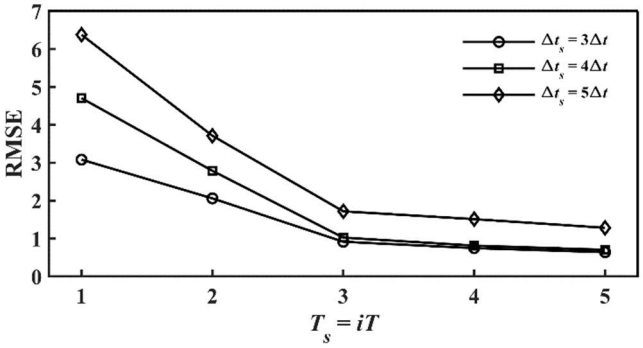

Figure 11 RMSE of the DMD reconstruction as a function of sampling interval with coverage period.

4.2. Modal energy and spectrum statistics

POD provides each mode's energy and time coefficient (see Eq. (4.2)), but does not directly provide the spectral information, which can be obtained by calculating the time coefficient's PSD. In contrast, the DMD provides direct access to each mode's eigenvalue λ_i, frequency f_i and amplitude α_i (see Eqs. (4.8) and (4.9)). Statistics on these critical parameters are given as follow.

4.2.1. POD modes

Figure 12 illustrates the relative energy of the first 25 POD modes and their cumulative energy. Overall, the energy of each mode decreases with increasing modal order. For the flow around the single and two crossing cylinders in 60° and 90° arrangements, the first mode has 84.55, 81.82 and 81.29% of total energy, respectively. In addition, the first 3, 3, 5 modes are needed to reach 90% of total energy, and the first 31, 29, 71 modes are needed to reach 99% of total energy, respectively. Statistics on modal energy show that

Preprints (www.preprints.org) | NOT PEER-REVIEWED | Posted: 10 May 2022 doi:10.20944/preprints202205.0137.v1

the presence or absence of DC and DC's arrangement significantly affects the convergence of the modal energy.

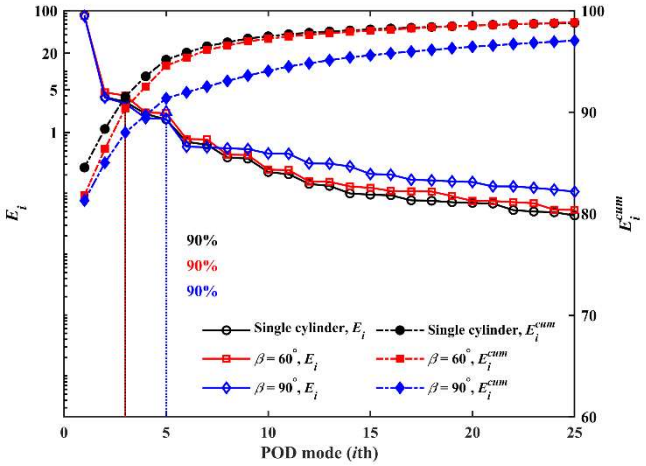

Figure 12 Relative and cumulative energy of POD modes.

The spectral peak distribution of the first 25 POD modes are further demonstrated in Figure 13, where the spectral peak value of each mode is normalised by its maximum value. Although most POD modes appear as multi-frequency coupling forms, the modal frequency peaks (black pixels) follow a linear function with modal order, and the frequency peaks of adjacent modes are the same in pairs. However, for the two crossing cylinders in 90° arrangement case, the linear relationship between modal order and frequency peaks is not as pronounced as the other two cases. For the studied three cases, the spectral peaks of these modes are approximately integer multiples of St = 0.16.

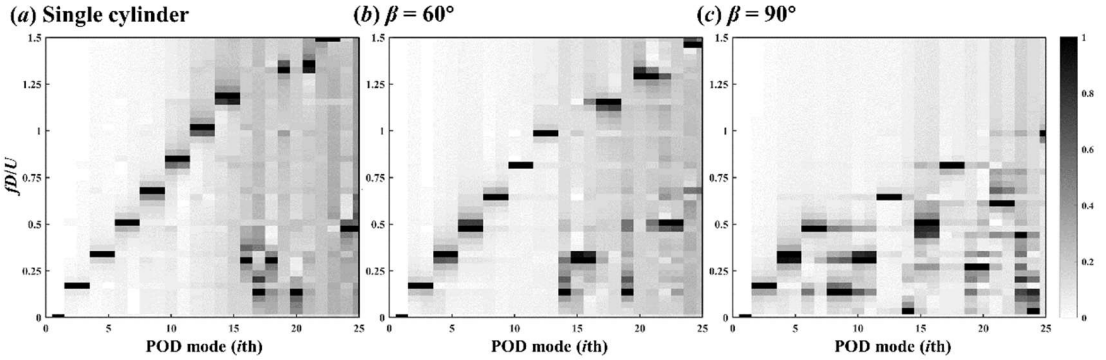

Figure 13 Spectral peak distribution of POD modes for the cases of the single cylinder (*a*) and two crossing cylinders in 60° (*b*) and 90° (*c*) arrangements.

4.2.2. DMD modes

To avoid the interference of transient or spurious mode with a high amplitude but a high decay rate, each DMD mode is sorted according to its dynamic factor, which is defined as $d_i = |\alpha_i| \times |\lambda_i|^{m-1}$. The dynamic factor can help identify the modes that make a prominent contribution to wake dynamics, similar to the sparsity-promoting DMD (SP DMD, Jovanović *et al.* 2014). Since the dynamic factor magnitude does not affect the analysis, the dynamic factor of each mode is normalised by the maximum dynamic factor in each case for the sake of consistency. The statistics of the modal frequency concerning the

Preprints (www.preprints.org) | NOT PEER-REVIEWED | Posted: 10 May 2022 doi:10.20944/preprints202205.0137.v1

normalised dynamic factor are shown in Figure 14, where the zero frequency modes are not considered and the first 15 modes are colored in red.

The spectra of DMD modes demonstrate that the modal contribution to the wake dynamics decreases with increasing modal frequency, and that the contribution of modes with St>1 is negligible. Similar to the POD modes' spectra in Figure 13, the frequencies of the crucial DMD mode are integer multiples of St = 0.16. However, more than one DMD mode exists around integer multiples of St = 0.16, especially for two crossing cylinder cases.

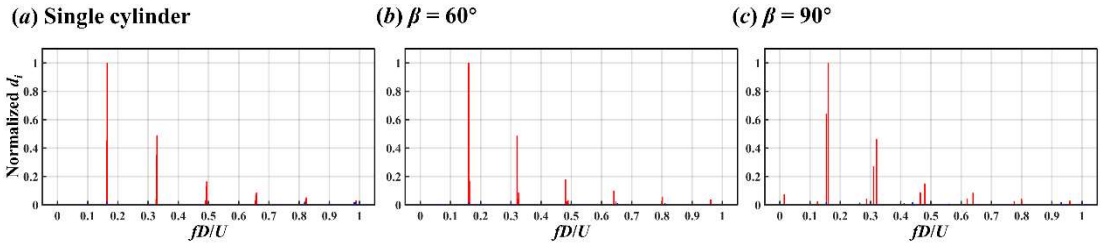

Figure 14 Spectral distribution of DMD modes for the cases of the single cylinder (*a*) and two crossing cylinders in 60° (*b*) and 90° (*c*) arrangements.

4.3. Modal results

This section will focus on the relationship between modal spatial patterns and frequencies. Note that the vorticity magnitude in the three-dimensional flow field is the quantity being analysed in this study, and only the spatial results on the y = 0 and z = 0 slices are shown below. In addition, since the mean flow modes with zero frequency present only a mean vorticity distribution but do not contribute to the flow's turbulence effect, these modes are not described in detail in the following section.

4.3.1. Single cylinder

The spatial patterns, time coefficients and PSDs of some important POD modes for the flow around the single cylinder are shown in Figure 15-Figure 17. Since adjacent POD modes have the same frequency peak (Figure 13), and their spatial patterns and time information are similar (not shown for conciseness), the first 18 POD modes are presented at intervals.

It is clear from Figure 17 that the 2nd, 4th, 6th, 8th, 10th, 12th, 14th POD modes have a relatively prominent spectral peak, corresponding to St = 0.16, 0.32, 0.48, 0.64, 0.8, 0.96, 1.12, respectively. For the 16th and 17th modes, there are substantial fluctuations in their time coefficients (Figure 16*h*, *i*) and these two modes have multiple spectral peaks (Figure 17 *h*, *i*).

The combination of Figure 15 and Figure 17 shows that spatial patterns of the modes with a spectral peak of odd multiples of St = 0.16 (St = i×0.16, i = 1, 3, 5, 7) are antisymmetric in space and those with a spectral peak of even multiples of St = 0.16 (St = i×0.16, i = 2, 4, 6) are spatially symmetric.

Because the vortex shedding frequency calculated by lift coefficient is St_L = 0.16 (see Figure 5*a*), the antisymmetric mode with a spectral peak of St = 0.16 is related to the vortex shedding from the cylinder. Similar to the decomposition results of rotating flows in Magionesi *et al.* (2018), the antisymmetric modes with a higher frequency peak (St = 0.48, 0.8, 1.12) differ only on spatial scale with respect to the mode with a low-frequency peak of St = 0.16. These antisymmetric patterns with no flow along the central axis of (y/D, z/D) = (0, 0) explain the absence of the St = 0.16, 0.48 signals in the KE spectrum of Figure 9.

Preprints (www.preprints.org) | NOT PEER-REVIEWED | Posted: 10 May 2022 doi:10.20944/preprints202205.0137.v1

The symmetric patterns are associated with the shift motion of shedding vortices during downstream evolution, and their flow signals are monitored in the KE spectrum of Figure 9. Similar to antisymmetric modes, the spatial scale of symmetry modes decreases with increasing frequency.

Although the 16th and 17th modes also represent the shedding vortices' shift motion and vortex shedding phenomena, respectively, their flow patterns are irregular in both space (Figure 15*h*, *i*) and time (Figure 16*h*, *i*) and, and they have multi-frequency characteristics (Figure 17*h*, *i*).

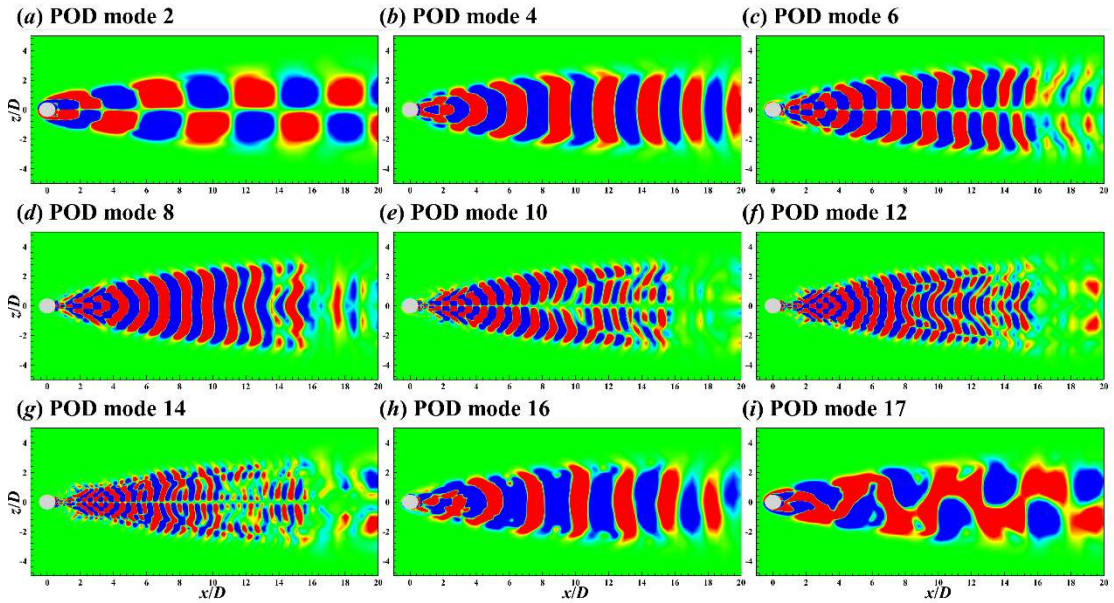

Figure 15 Contours of the 2nd (*a*), 4th (*b*), 6th (*c*), 8th (*d*), 10th (*e*), 12th (*f*), 14th (*g*), 16th (*h*), 17th (*i*) POD modes on the *xz* plane for the flow around the single cylinder.

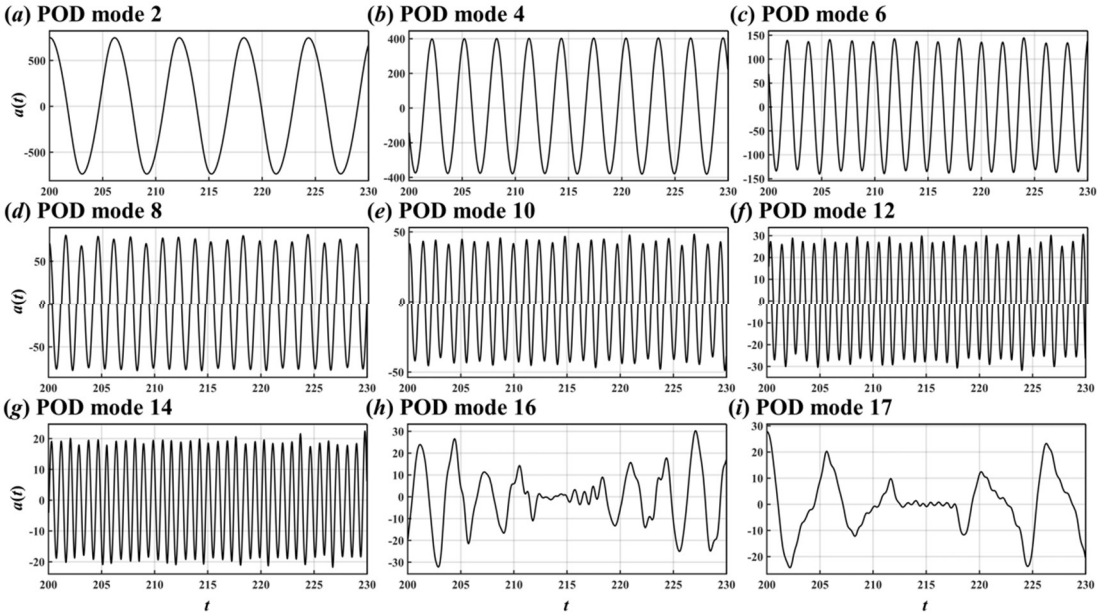

Figure 16 Time coefficients of the 2nd (*a*), 4th (*b*), 6th (*c*), 8th (*d*), 10th (*e*), 12th (*f*), 14th (*g*), 16th (*h*), 17th (*i*) POD modes for the flow around the single cylinder.

Preprints (www.preprints.org) | NOT PEER-REVIEWED | Posted: 10 May 2022 doi:10.20944/preprints202205.0137.v1

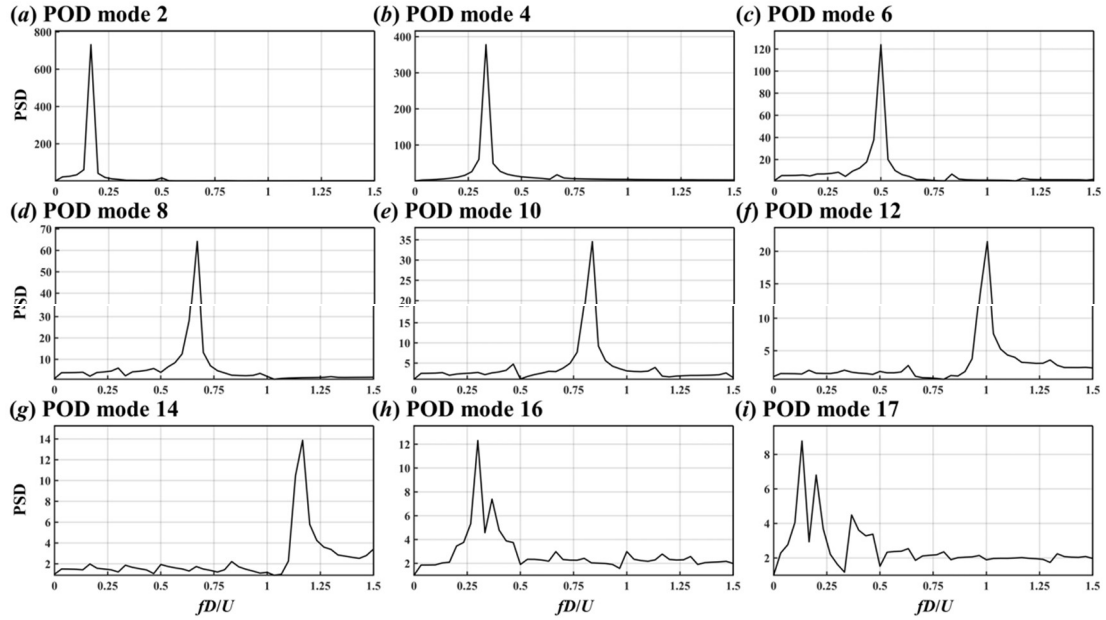

Figure 17 PSDs of the 2nd (*a*), 4th (*b*), 6th (*c*), 8th (*d*), 10th (*e*), 12th (*f*), 14th (*g*), 16th (*h*), 17th (*i*) POD modes for the flow around the single cylinder.

DMD modes are sorted according to their corresponding dynamic factors (see Figure 14*a*), and Figure 18 and Figure 19 show the first 9 DMD modes and their corresponding time coefficients, respectively. Unlike POD modes, DMD modes do not fluctuate in time, and their time coefficients increase or decrease exponentially (Eq. (4.6)) or remain constant over time (see Figure 19).

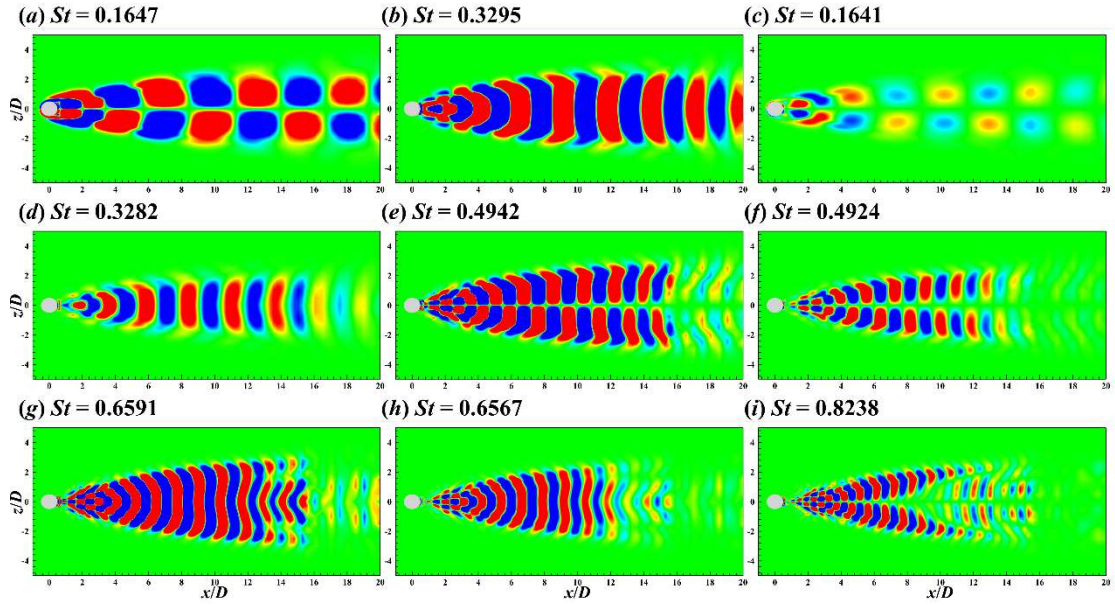

Figure 18 Contours of the St = 0.1647 (*a*), 0.3295 (*b*), 0.1641 (*c*), 0.3282 (*d*), 0.4942 (*e*), 0.4924 (*f*), 0.6591 (*g*), 0.6567 (*h*), 0.8238 (*i*) DMD modes on the xz plane for the flow around the single cylinder.

Two DMD modes with close frequencies occur in pairs around St = 0.165, 0.33, 0.49, 0.66 (i.e. St = 0.1647 and 0.1641, 0.3295 and 0.3282, 0.4942 and 0.4924, 0.6591 and 0.6567), and the spatial characteristics between the two modes are similar. Considering the three-

Preprints (www.preprints.org) | NOT PEER-REVIEWED | Posted: 10 May 2022 doi:10.20944/preprints202205.0137.v1

dimensional numerical simulation results, when a cylinder is long, there is a small frequency difference between the vortex shedding from two ends of the cylinder. Because DMD is sensitive in identifying flow phenomena with a single-frequency characteristic, similar DMD modes emerge in pairs in the three-dimensional flow around the single cylinder in this study, while this phenomenon does not occur in the two-dimensional flow case (Kutz *et al.* 2016).

The spatial patterns of DMD modes are consistent with those of POD modes, and higher frequency DMD modes are no longer shown here.

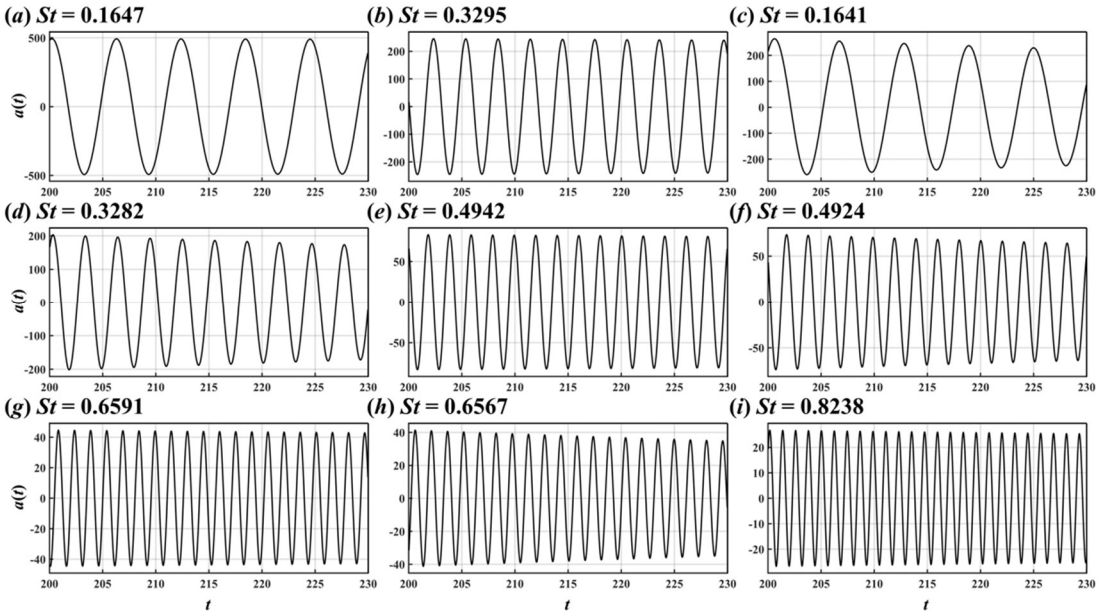

Figure 19 Time coefficients of the St = 0.1647 (*a*), 0.3295 (*b*), 0.1641 (*c*), 0.3282 (*d*), 0.4942 (*e*), 0.4924 (*f*), 0.6591 (*g*), 0.6567 (*h*), 0.8238 (*i*) DMD modes for the flow around the single cylinder.

4.3.2. Two crossing cylinders in 60° arrangement

For the two crossing cylinder cases, in addition to the modal contours on the xz plane, the contours of modes on the xy plane are also presented to show the global wake patterns of UC. The first 18 POD modes for the case of two crossing cylinders in 60° arrangement are shown at intervals in Figure 20-Figure 23.

For the flow around the UC, it can be seen from the 2nd, 4th, 6th, 8th, 10th, 12th, 18th POD modes in Figure 20 that the modal patterns in the range of $0.5<x/D<4.5$ are the same as that of the corresponding modes in the single cylinder case (Figure 15). When the shedding vortices from UC centre encounter the DC, these modes' symmetry and anti-symmetry remain unchanged (see Figure 20 and Figure 21). Furthermore, because the cross section of the DC arranged at 60° on the xz plane is an ellipse, diffraction of the flow cause the DC wake to expand in the z direction (Figure 20).

As can be seen from Figure 20(*a*) and Figure 21(*a*), for the mode with a spectral peak of St = 0.16, its pattern is always antisymmetric on both xz and xy planes, corresponding to the unchanged lift force frequency along the spanwise direction of UC and DC (Figure 5*b*, *d*). As for the KE spectra in Figure 10(*b*, *c*), the spectral peaks of St = 0.16 and 0.48 around the crossing point of lines 3 are caused by the antisymmetric flow patterns from DC centre, and those of lines 4 are caused by the antisymmetric patterns from UC centre.

Preprints (www.preprints.org) | NOT PEER-REVIEWED | Posted: 10 May 2022 doi:10.20944/preprints202205.0137.v1

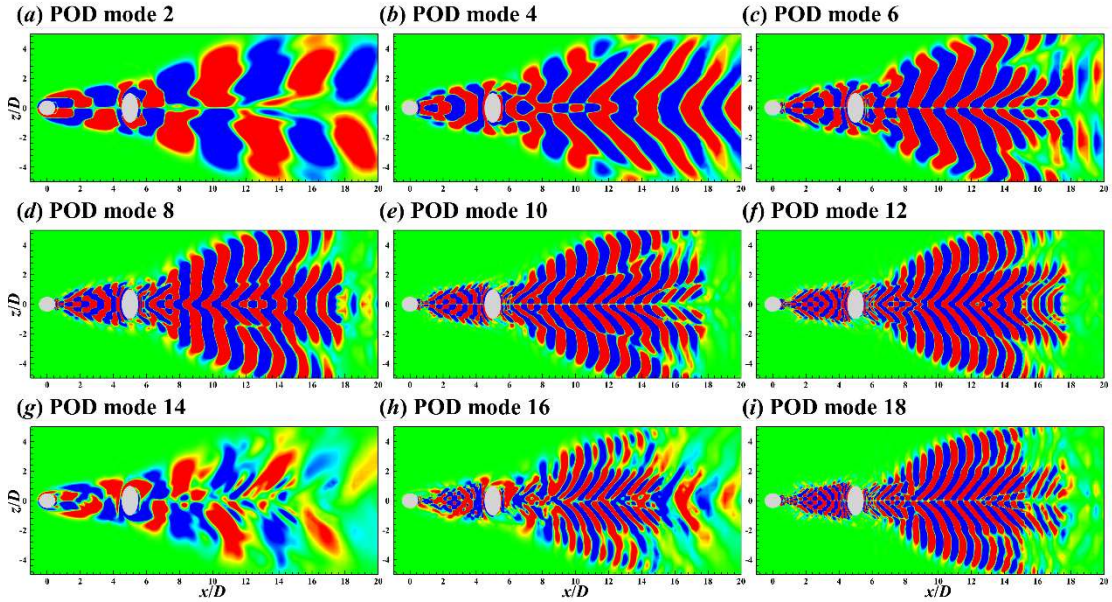

Figure 20 Contours of the 2nd (*a*), 4th (*b*), 6th (*c*), 8th (*d*), 10th (*e*), 12th (*f*), 14th (*g*), 16th (*h*), 18th (*i*) POD modes on the *xz* plane for the flow around the two crossing cylinders in 60° arrangement.

391

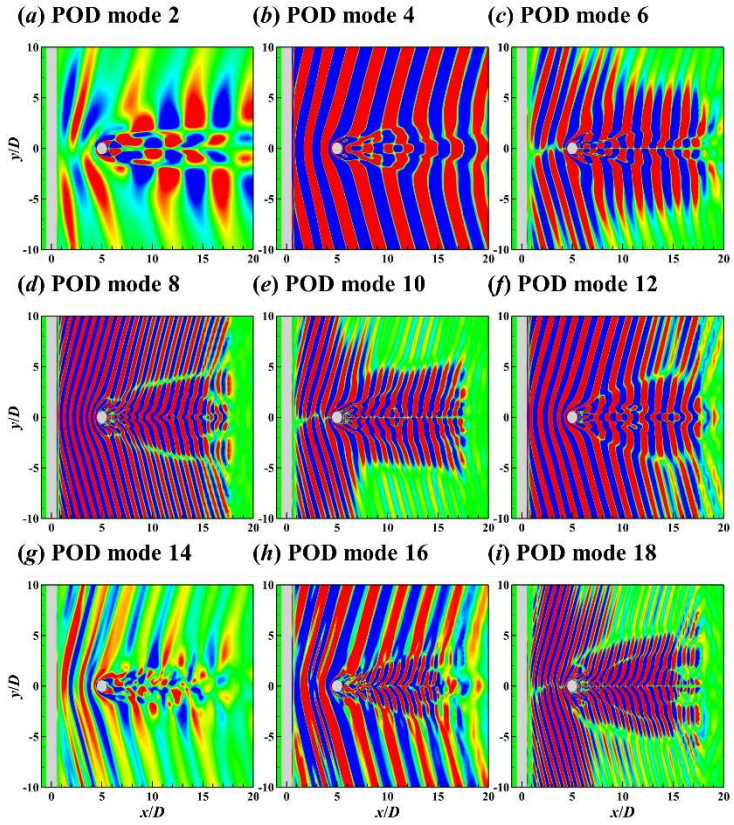

Figure 21 Contours of the 2nd (*a*), 4th (*b*), 6th (*c*), 8th (*d*), 10th (*e*), 12th (*f*), 14th (*g*), 16th (*h*), 18th (*i*) POD modes on the *xy* plane for the flow around the two crossing cylinders in 60° arrangement.

392

393

Preprints (www.preprints.org) | NOT PEER-REVIEWED | Posted: 10 May 2022 doi:10.20944/preprints202205.0137.v1

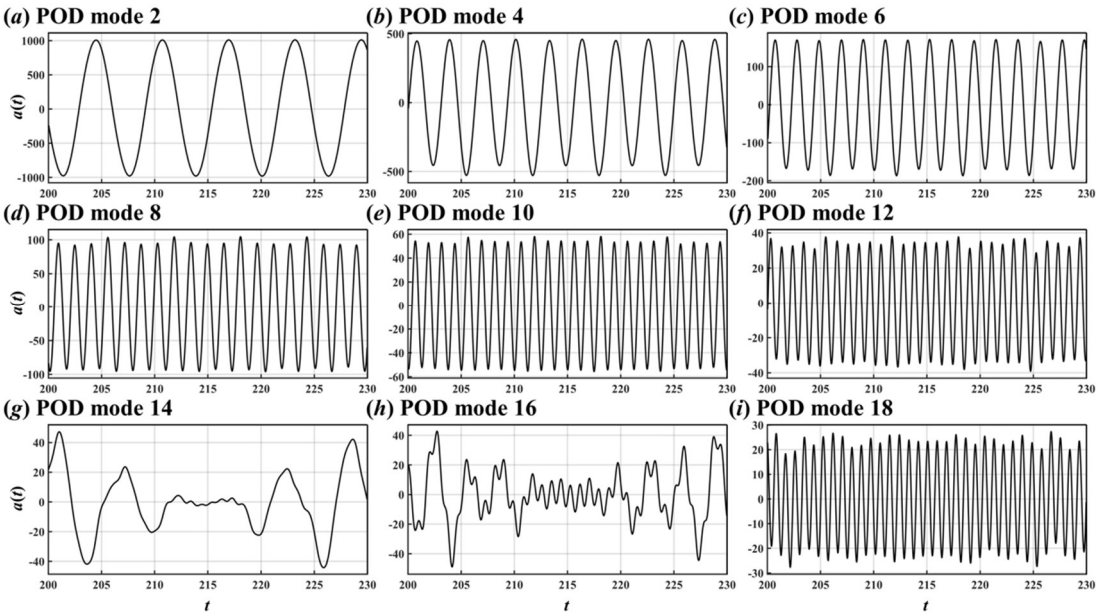

Figure 22 Time coefficients of the 2nd (*a*), 4th (*b*), 6th (*c*), 8th (*d*), 10th (*e*), 12th (*f*), 14th (*g*), 16th (*h*), 18th (*i*) POD modes for the flow around the two crossing cylinders in 60° arrangement.

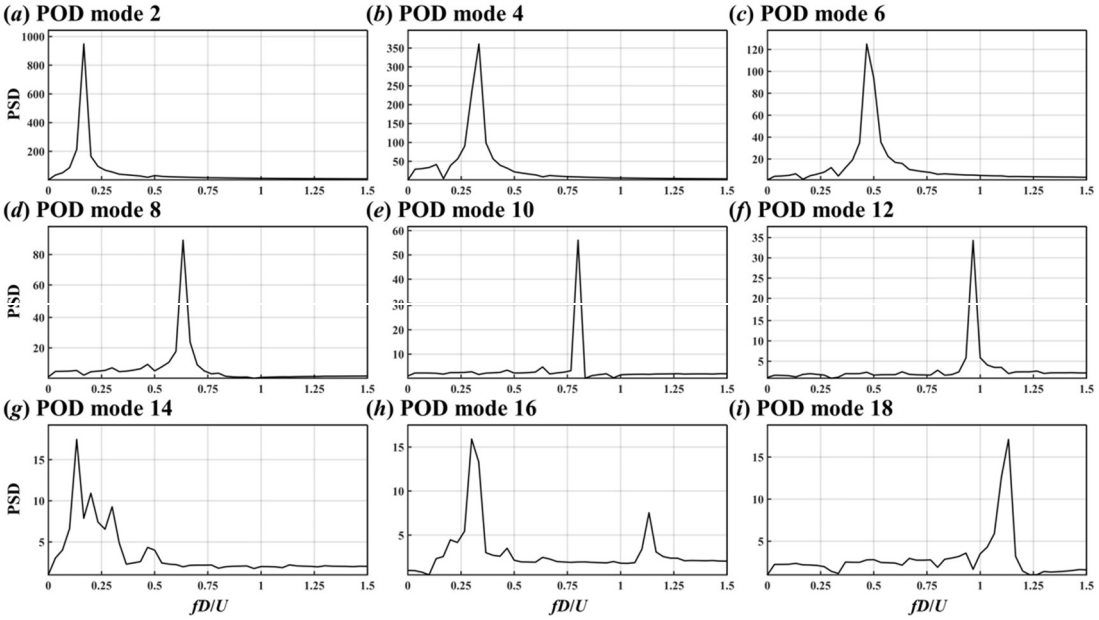

Figure 23 PSDs of the 2nd (*a*), 4th (*b*), 6th (*c*), 8th (*d*), 10th (*e*), 12th (*f*), 14th (*g*), 16th (*h*), 18th (*i*) POD modes for the flow around the two crossing cylinders in 60° arrangement.

The spatial and temporal results of DMD modes are shown in Figure 24-Figure 26, where the spatial patterns of DMD modes are similar to those of POD modes but DMD modes have a single-frequency characteristic. Interestingly, three similar DMD modes appear around St = 0.32, and their frequencies are St = 0.3204, 0.3258, 0.3227 (see Figure 24*b*, *f*, *h* and Figure 25*b*, *f*, *h*). In addition to the frequency difference between the vortex shedding from two ends of the cylinder explained above, the difference in vortex shedding frequency between UC and DC is responsible for the appearance of more than two similar DMD modes.

Preprints (www.preprints.org) | NOT PEER-REVIEWED | Posted: 10 May 2022 doi:10.20944/preprints202205.0137.v1

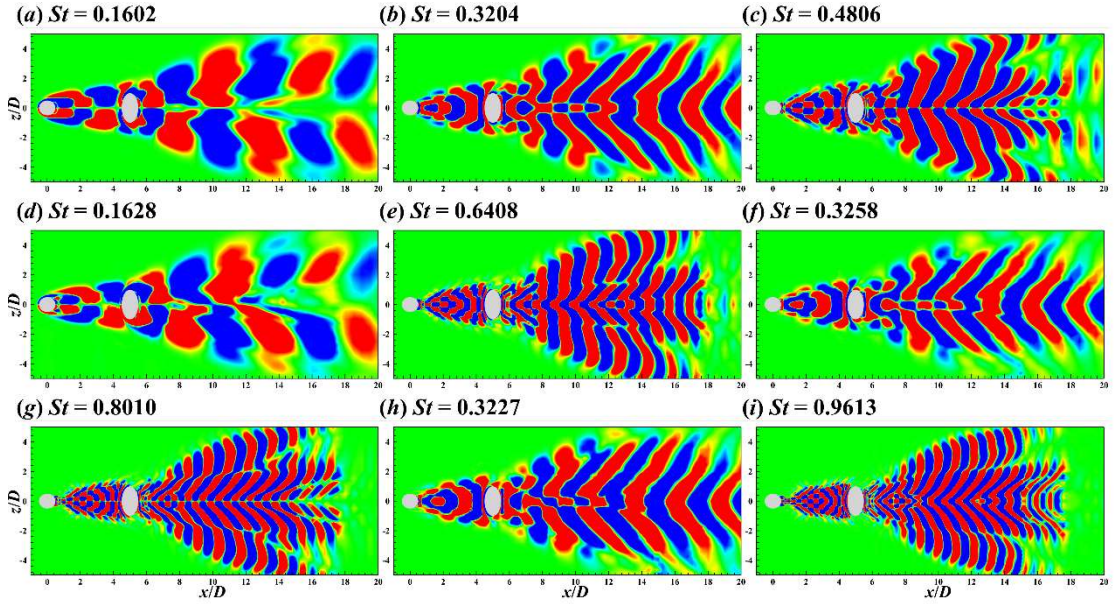

Figure 24 Contours of the St = 0.1602 (*a*), 0.3204 (*b*), 0.4806 (*c*), 0.1628 (*d*), 0.6408 (*e*), 0.3258 (*f*), 0.8010 (*g*), 0.3227 (*h*), 0.9613 (*i*) DMD modes on the xz plane for the flow around the two crossing cylinders in 60° arrangement.

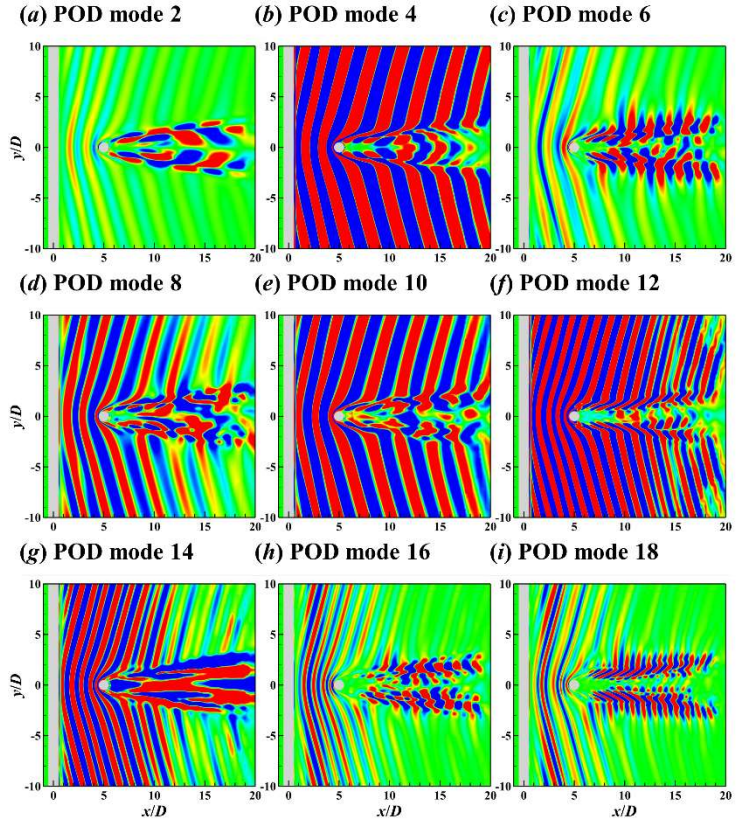

Figure 25 Contours of the St = 0.1602 (*a*), 0.3204 (*b*), 0.4806 (*c*), 0.1628 (*d*), 0.6408 (*e*), 0.3258 (*f*), 0.8010 (*g*), 0.3227 (*h*), 0.9613 (*i*) DMD modes on the xy plane for the flow around the two crossing cylinders in 60° arrangement.

 doi:10.20944/preprints202205.0137.v1

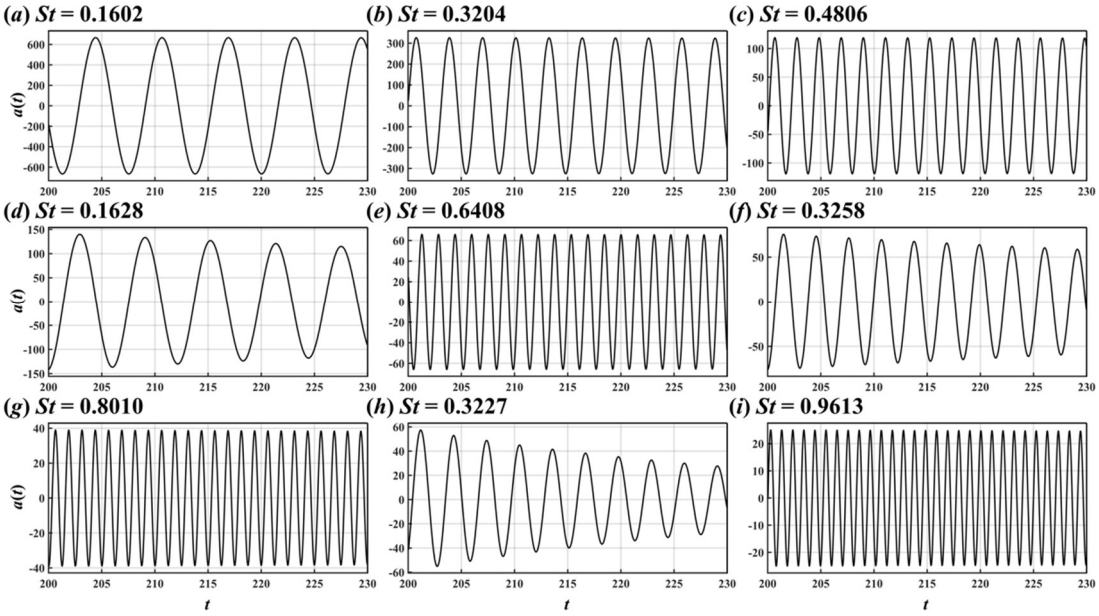

Figure 26 Time coefficients of the St = 0.1602 (*a*), 0.3204 (*b*), 0.4806 (*c*), 0.1628 (*d*), 0.6408 (*e*), 0.3258 (*f*), 0.8010 (*g*), 0.3227 (*h*), 0.9613 (*i*) DMD modes for the flow around the two crossing cylinders in 60° arrangement.

4.3.3. Two crossing cylinders in 90° arrangement

The first 18 POD modes in the two crossing cylinders in 90° arrangement case are shown at intervals in Figure 27-Figure 30. The POD modes' multi-frequency couplings are more severe than that of the other two cases (Figure 30). Enhanced multi-frequency coupling and slow energy convergence (Figure 12) are caused by the blockage of DC on the shedding vortices from UC and the resulting vortex breakdown. In other words, when encountering DC in 90° arrangement, large-scale wake vortices from UC centre break down into numerous small-scale vortices, which is not conducive for POD to decompose the flow field.

Preprints (www.preprints.org) | NOT PEER-REVIEWED | Posted: 10 May 2022 doi:10.20944/preprints202205.0137.v1

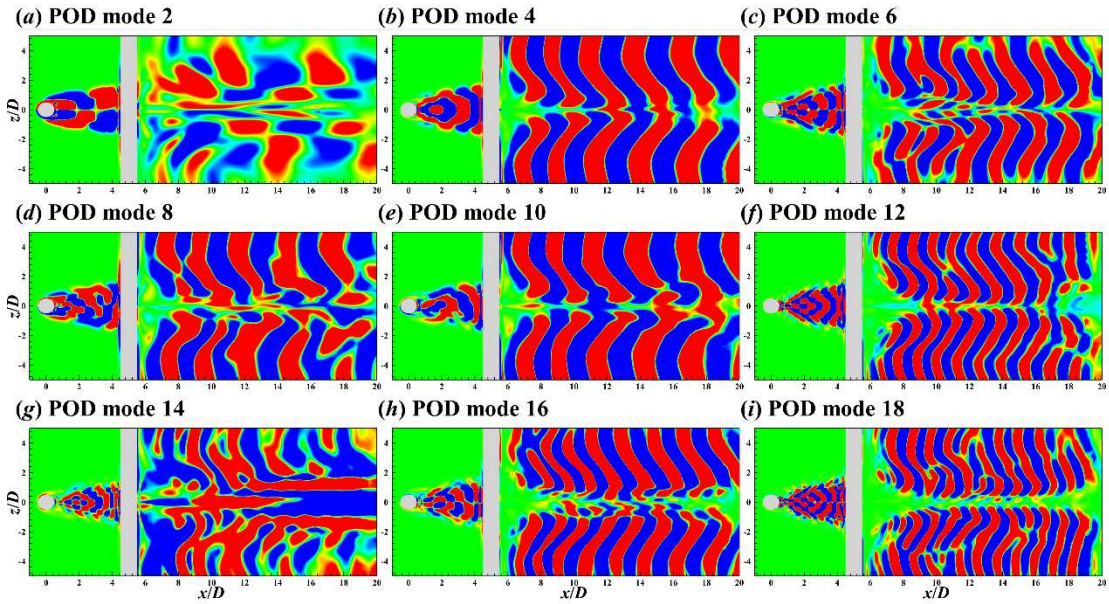

Figure 27 Contours of the 2nd (*a*), 4th (*b*), 6th (*c*), 8th (*d*), 10th (*e*), 12th (*f*), 14th (*g*), 16th (*h*), 18th (*i*) POD modes on the *xz* plane for the flow around the two crossing cylinders in 90° arrangement.

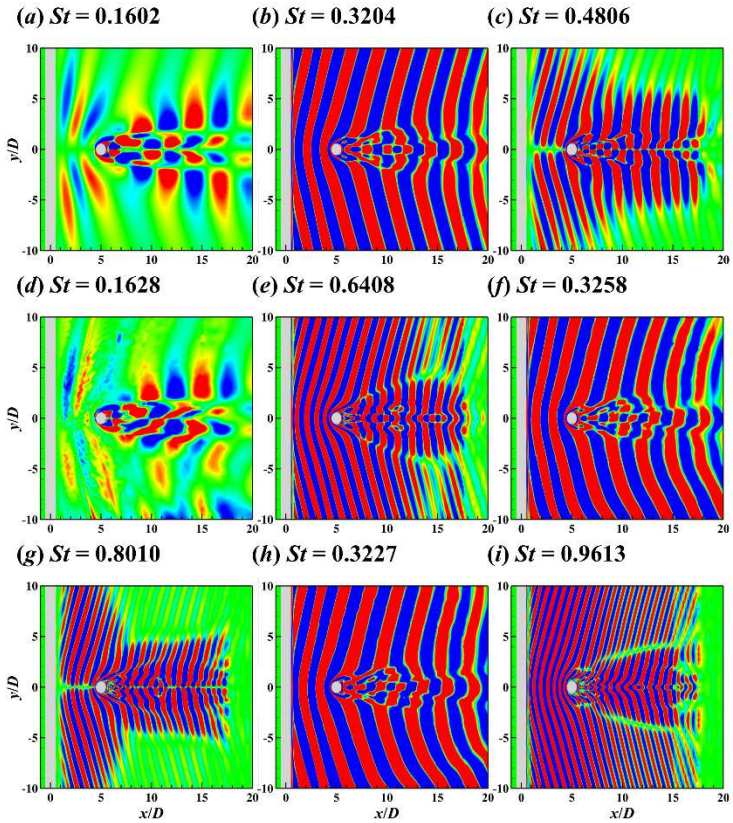

Figure 28 Contours of the 2nd (*a*), 4th (*b*), 6th (*c*), 8th (*d*), 10th (*e*), 12th (*f*), 14th (*g*), 16th (*h*), 18th (*i*) POD modes on the *xy* plane for the flow around the two crossing cylinders in 90° arrangement.

Preprints (www.preprints.org) | NOT PEER-REVIEWED | Posted: 10 May 2022 doi:10.20944/preprints202205.0137.v1

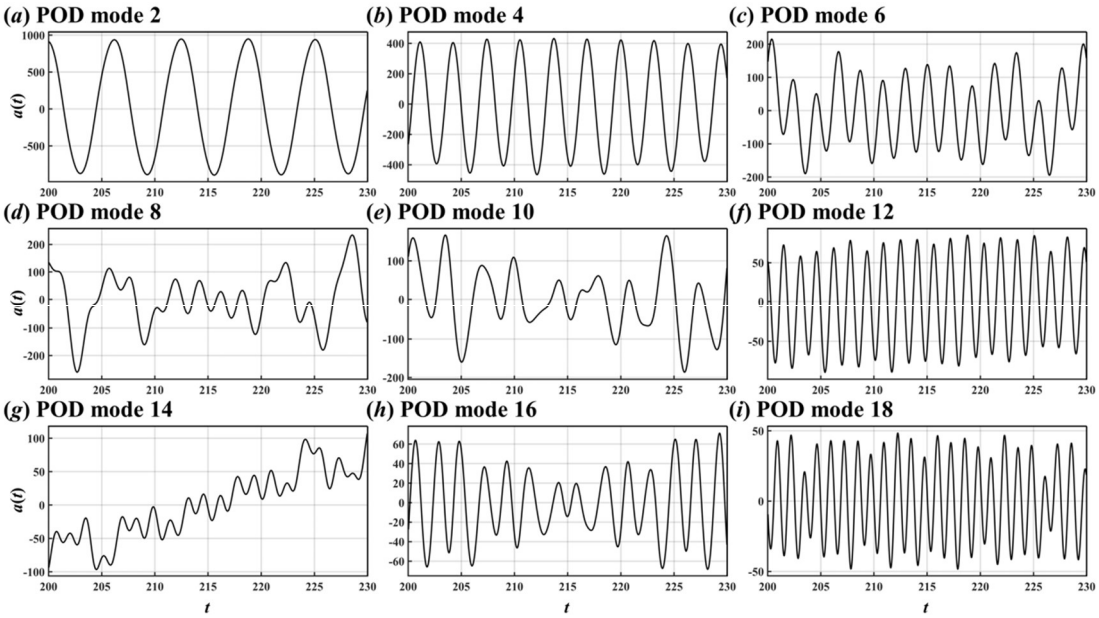

Figure 29 Time coefficients of the 2nd (*a*), 4th (*b*), 6th (*c*), 8th (*d*), 10th (*e*), 12th (*f*), 14th (*g*), 16th (*h*), 18th (*i*) POD modes for the flow around the two crossing cylinders in 90° arrangement.

421

422

423

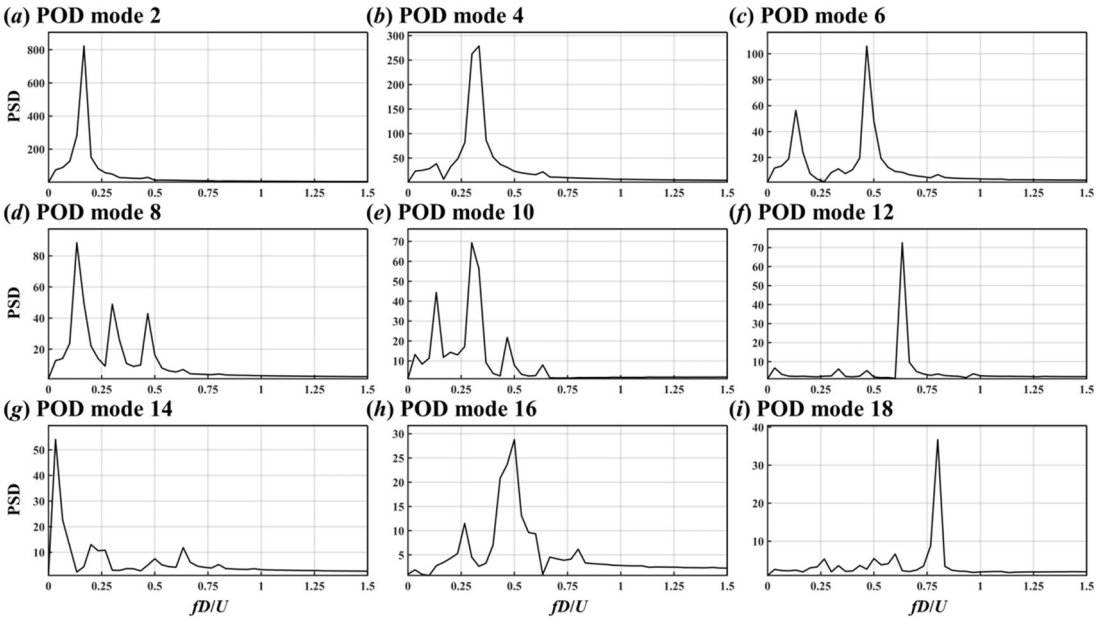

Figure 30 PSDs of the 2nd (*a*), 4th (*b*), 6th (*c*), 8th (*d*), 10th (*e*), 12th (*f*), 14th (*g*), 16th (*h*), 18th (*i*) POD modes for the flow around the two crossing cylinders in 90° arrangement.

424

Preprints (www.preprints.org) | NOT PEER-REVIEWED | Posted: 10 May 2022 doi:10.20944/preprints202205.0137.v1

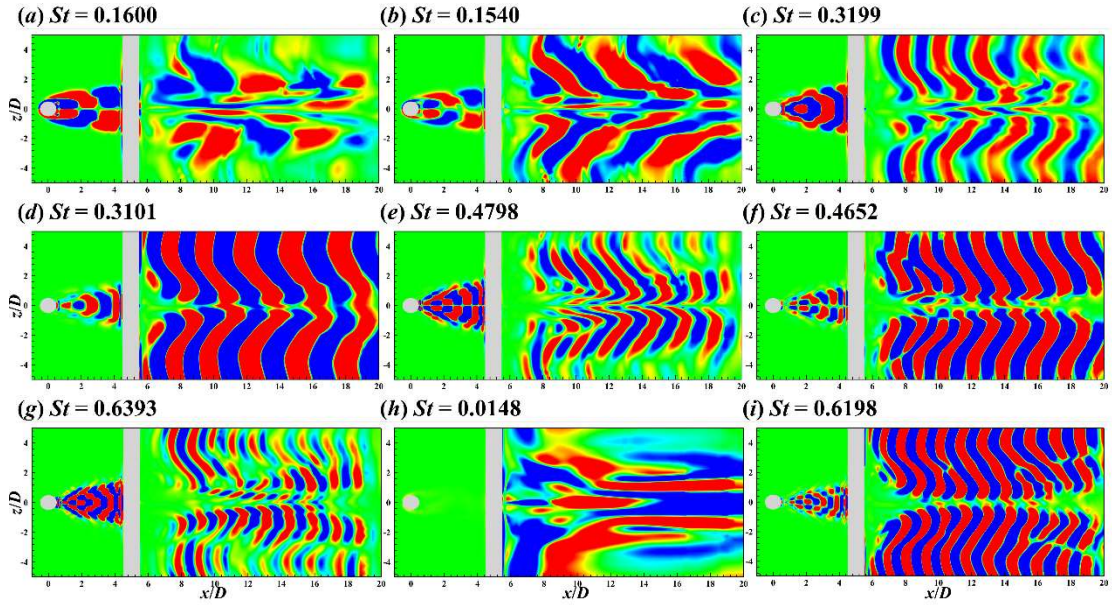

Figure 31 Contours of the St = 0.1600 (*a*), 0.1540 (*b*), 0.3199 (*c*), 0.3101 (*d*), 0.4798 (*e*), 0.4652 (*f*), 0.6393 (*g*), 0.0148 (*h*), 0.6198 (*i*) DMD modes on the xz plane for the flow around the two crossing cylinders in 90° arrangement.

Figure 31-Figure 33 show the first 9 DMD modes of flow around two cylinders in 90° arrangement. Compared with POD, DMD is a practical tool in the severe destabilisation case due to its single-frequency characteristic. For the flow around the crossing point, the flow patterns of symmetric modes are distinctive on both xy and xz planes, e.g. St = 0.3101 DMD mode (see Figure 31*d* and Figure 32*d*). But for the antisymmetric modes, the distinctive flow patterns of the wake vortices from UC and DC appear on different planes. For instance, for the St = 0.1600 DMD mode, the antisymmetric flow pattern of UC wake is significant on the xz plane (see Figure 27*a*), but that of DC wake is significant on the xy plane (see Figure 28*a*).

Preprints (www.preprints.org) | NOT PEER-REVIEWED | Posted: 10 May 2022 doi:10.20944/preprints202205.0137.v1

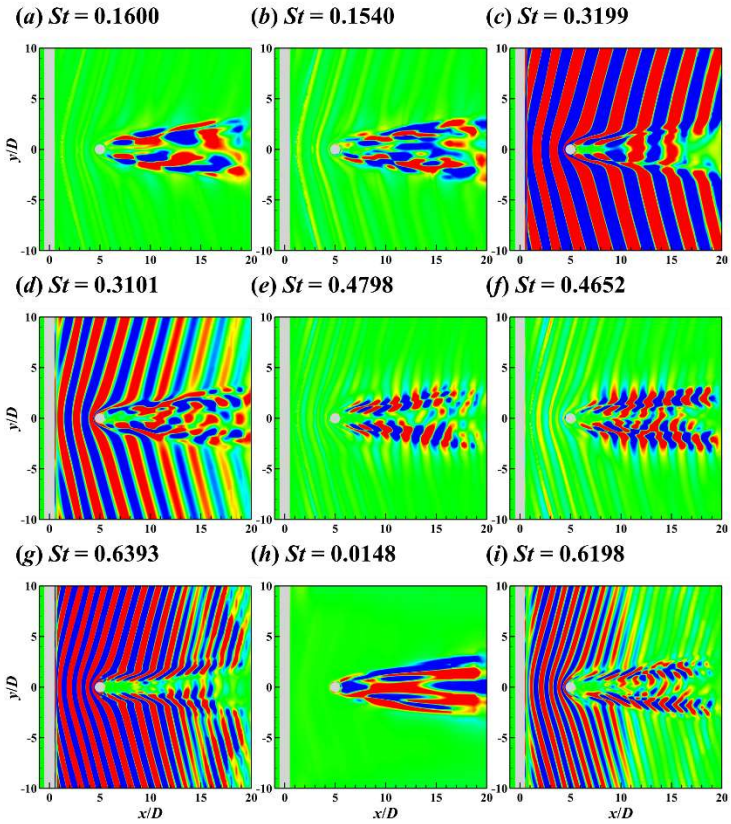

Figure 32 Contours of the St = 0.1600 (*a*), 0.1540 (*b*), 0.3199 (*c*), 0.3101 (*d*), 0.4798 (*e*), 0.4652 (*f*), 0.6393 (*g*), 0.0148 (*h*), 0.6198 (*i*) DMD modes on the xy plane for the flow around the two crossing cylinders in 90° arrangement.

436

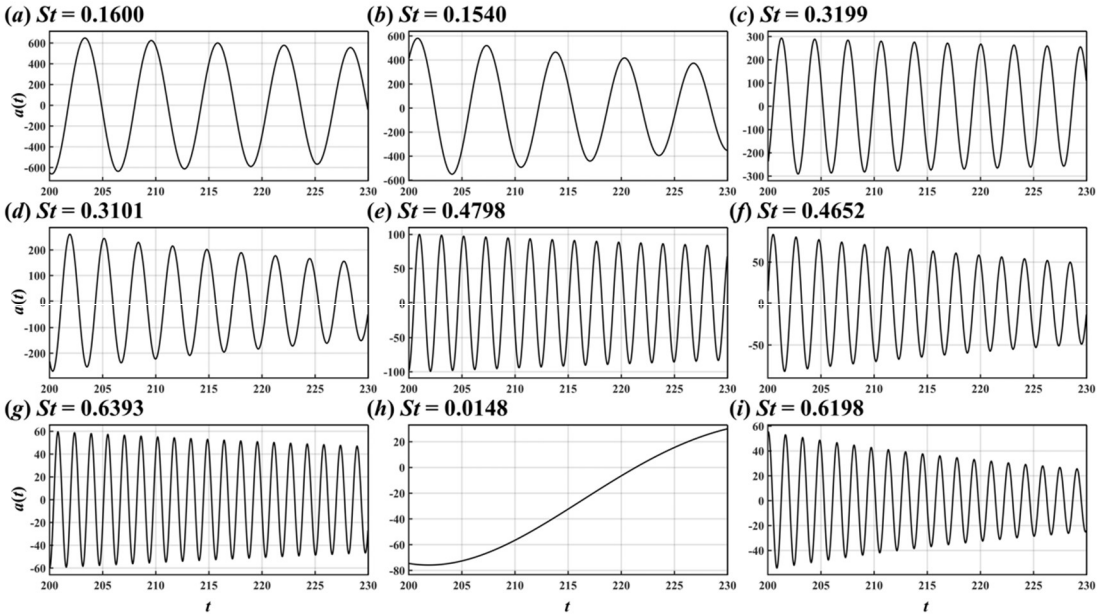

Figure 33 Time coefficients of the St = 0.1600 (*a*), 0.1540 (*b*), 0.3199 (*c*), 0.3101 (*d*), 0.4798 (*e*), 0.4652 (*f*), 0.6393 (*g*), 0.0148 (*h*), 0.6198 (*i*) DMD modes for the flow around the two crossing cylinders in 90° arrangement.

437

Although UC wake's induction and DC's blockage effect (Zhao & Lu 2018) cause the flow around DC centre to move downstream along approximately $|L/D| = 1$ (Figure 8*c*), the antisymmetric vortex shedding modes and symmetric shift motion modes still exist.

For the antisymmetric mode with $St = 0.1600$ (Figure 32*a*), the shedding vortices from DC centre become narrower in the y direction due to UC wake's interference and DC's blockage effect. For the symmetric mode with $St = 0.3199$ (Figure 31*c* and Figure 32*c*), symmetric flow patterns are not found on the central axis ($y/D = 0$, $z/D = 0$) in the range of $x/D = 5.5$-9 due to the blockage of DC. In addition, there is a low-frequency flow pattern in the wake of DC centre (see Figure 31*h* and Figure 32*h*). The low-frequency mode is related to the low-speed flow under the shadowing effect of DC.

5. Summary

This study employs modal decomposition techniques, including POD and DMD, to investigate the wake patterns past single and two crossing cylinder configurations at $Re = 100$. The two crossing cylinders are arranged at 60° and 90° with a gap ratio $G = 4$. The numerical simulation is conducted using DNS.

We foucus on the effect of DC's arrangement on the wake patterns around the crossing point. For the DC in 60 arrangement, the shedding vortices from UC centre undergo diffraction after passing through the DC. However, for the DC in 90 arrangement, due to the DC's blockage effect, the wake vortices from UC centre break down when encountering the DC.

POD and DMD have their own advantages. For the stable flow, i.e. flow around the single and two crossing cylinders in 60° arrangement, POD can successfully extract the modes that contribute most to the wake dynamics, and these modes have a single, prominent spectral peak. Due to the frequency sensitivity, DMD may capture the single-frequency modes with similar frequencies, temporal information and spatial patterns. This is caused by the frequency difference between the vortex shedding from two ends of the cylinder, or the frequency difference between the wake of UC and DC. For the severely destabilised flow, i.e. flow around two crossing cylinders in 90° arrangement, POD is not practical for analysis due to the enhanced multi-frequency coupling.

Both POD and DMD identify spatially antisymmetric and symmetric wake patterns for the studied three cases. Antisymmetric modes are associated with the vortex shedding phenomenon in the flow field, and these modes' frequencies are odd multiples of cylinders' lift force frequency. Symmetric modes are associated with the shift motion of shedding vortices during downstream evolution, and these modes' frequencies are even multiples of cylinders' lift force frequency. The spatial scale of the above modes decreases with increasing frequency.

For the flow around the DC in 90° arrangement, both symmetric and antisymmetric modes have significant deformation due to the interference of the UC wake and the blockage effect of DC. In addition, a low-frequency mode is found in the wake of DC centre, which is related to the shadowing effect of DC.

For the three-dimensional flow, the cylinder length seems to affect the DMD analysis, in the next work we will focus on this subject.

Funding: The reported study was funded by Russian Foundation for Basic Research (RFBR, Proj. No. 21-57-53019) and National Natural Science Foundation of China (NSFC, Proj. No. 52111530047).

Reference

Bagheri, S., 2013. Koopman-mode decomposition of the cylinder wake. Journal of Fluid Mechanics 726, 596-623.

Bai, H.L., Alam, M.M., Gao, N., Lin, Y.F., 2019. The near wake of sinusoidal wavy cylinders: Three-dimensional POD analyses. International Journal of Heat and Fluid Flow 75, 256-277.

Chen, K.K., Tu, J.H., Rowley, C.W., 2012. Variants of Dynamic Mode Decomposition: Boundary Condition, Koopman, and Fourier Analyses. 22, 887-915.

Deng, J., Ren, A.L., Shao, X.M., 2007. The flow between a stationary cylinder and a downstream elastic cylinder in cruciform arrangement. Journal of Fluids and Structures 23, 715-731.

Desoer, C., Wang, Y., 1980. On the generalized Nyquist stability criterion.

Jauvtis, N., Williamson, C.H.K., 2003. Vortex-induced vibration of a cylinder with two degrees of freedom. Journal of Fluids and Structures 17, 1035-1042.

Jeong, J., Hussain, F., 1995. On the identification of a vortex. J. Fluid Mech. 332, 339-363.

Jovanović, M.R., Schmid, P.J., Nichols, J.W., 2014. Sparsity-promoting dynamic mode decomposition. Physics of Fluids 26, 024103.

Kato, N., Koide, M., Takahashi, T., Shirakash, M., 2012. VIVs of a circular cylinder with a downstream strip-plate in cruciform arrangement. Journal of Fluids and Structures 30, 97-114.

Kutz, J.N., Brunton, S.L., Brunton, B.W., Proctor, J.L., 2016. Dynamic Mode Decomposition: Data-Driven Modeling of Complex Systems. SIAM.

Lumley, J.L., 1970. Stochastic Tools in Turbulence

Magionesi, F., Dubbioso, G., Muscari, R., Di Mascio, A., 2018. Modal analysis of the wake past a marine propeller. Journal of Fluid Mechanics 855, 469-502.

Naderi, M.H., Eivazi, H., Esfahanian, V., 2019. New method for dynamic mode decomposition of flows over moving structures based on machine learning (hybrid dynamic mode decomposition). Physics of Fluids 31, 127102.

Nguyen, T., Koide, M., Yamada, S., Takahashi, T., Shirakashi, M., 2012. Influence of mass and damping ratios on VIVs of a cylinder with a downstream counterpart in cruciform arrangement. Journal of Fluids and Structures 28, 40-55.

Noack, B.R., Stankiewicz, W., Morzyński, M., Schmid, P.J., 2016. Recursive dynamic mode decomposition of transient and post-transient wake flows. Journal of Fluid Mechanics 809, 843-872.

Rowley, C., Dawson, S., 2017. Model Reduction for Flow Analysis and Control. Annual Review of Fluid Mechanics 49.

Sakai, M., Sunada, Y., Imamura, T., Rinoie, K., 2014. Experimental and Numerical Flow Analysis around Circular Cylinders Using POD and DMD, 44th AIAA Fluid Dynamics Conference. American Institute of Aeronautics and Astronautics.

Sakai, M., Sunada, Y., Imamura, T., Rinoie, K., 2015. Experimental and Numerical Studies on Flow behind a Circular Cylinder Based on POD and DMD. TRANSACTIONS OF THE JAPAN SOCIETY FOR AERONAUTICAL AND SPACE SCIENCES 58, 100-107.

Scherl, I., Strom, B., Shang, J., Williams, O., Polagye, B., Brunton, S., 2020. Robust principal component analysis for modal decomposition of corrupt fluid flows. Physical Review Fluids 5.

Schmid, P.J., 2010. Dynamic Mode Decomposition of numerical and experimental data. Journal of Fluid Mechanics 656, 5-28.

Sirisup, S., Tomkratoke, S., 2009. Proper Orthogonal Decomposition of Unsteady Heat Transfer from Staggered Cylinders at Moderate Reynolds Numbers, in: Choi, H., Choi, H.G., Yoo, J.Y. (Eds.), Computational Fluid Dynamics 2008. Springer Berlin Heidelberg, Berlin, Heidelberg, pp. 763-769.

Sumner, D., 2010. Two circular cylinders in cross-flow: A review. Journal of Fluids and Structures 26, 849-899.

Taira, K., Brunton, S.L., Dawson, S.T.M., Rowley, C.W., Colonius, T., McKeon, B.J., Schmidt, O.T., Gordeyev, S., Theofilis, V., Ukeiley, L.S., 2017. Modal Analysis of Fluid Flows: An Overview. AIAA Journal 55, 1-29.

Tong, F., Cheng, L., Zhao, M., 2015. Numerical simulations of steady flow past two cylinders in staggered arrangements. Journal of Fluid Mechanics 765, 114-149.

Tu, J., Rowley, C., Luchtenburg, D., Brunton, S., Kutz, J., 2013. On Dynamic Mode Decomposition: Theory and Applications. Journal of Computational Dynamics 1.

 doi:10.20944/preprints202205.0137.v1

Tu, J.H., Rowley, C.W., Kutz, J.N., Shang, J.K., 2014. Spectral analysis of fluid flows using sub-Nyquist-rate PIV data. Experiments in Fluids 55, 1805.

Wall, M., Rechtsteiner, A., Rocha, L., 2002. Singular Value Decomposition and Principal Component Analysis. In A Practical Approach to Microarray Data Analysis 5.

Wang, F., Zheng, X., Hao, J., Bai, H., 2020. Numerical Analysis of the Flow around Two Square Cylinders in a Tandem Arrangement with Different Spacing Ratios Based on POD and DMD Methods. Processes 8, 903.

Wang, H.F., Cao, H.L., Zhou, Y., 2014. POD analysis of a finite-length cylinder near wake. Experiments in Fluids 55, 1790.

Zhang, Q., Liu, Y., Wang, S., 2014. The identification of coherent structures using proper orthogonal decomposition and dynamic mode decomposition. Journal of Fluids and Structures 49, 53-72.

Zhao, M., Cheng, L., Zhou, T., 2009. Direct numerical simulation of three-dimensional flow past a yawed circular cylinder of infinite length. Journal of Fluids and Structures 25, 831-847.

Zhao, M., Lu, L., 2018. Numerical simulation of flow past two circular cylinders in cruciform arrangement. Journal of Fluid Mechanics 848, 1013-1039.

Zhao, Y., Zhao, M., Li, X., Liu, Z., Du, J., 2019. A modified proper orthogonal decomposition method for flow dynamic analysis. Computers & Fluids 182, 28-36.

Zhou, Y., Mahbub Alam, M., 2016. Wake of two interacting circular cylinders: A review. International Journal of Heat and Fluid Flow 62, 510-537.